Dependence of the NS conductance on the valley polarisation of edge states in graphene

I.M. Flór

to obtain the Bachelor of Science in Applied Physics
at the Delft University of Technology.

Student number:	4486870,	
Project duration:	April 23, 2019 – September 23, 2019,	
Thesis committee:	Assoc. Prof. A. R. (Anton) Akhmerov,	TU Delft, supervisor/examiner,
	Dr. C–X. (Chun–Xiao) Liu,	TU Delft, supervisor,
	Dr. M. T. (Michael) Wimmer,	TU Delft, second examiner,
Group:	Department of Quantum Nanoscience, Theoretical Physics (Quantum Tinkerer).	

Abstract

The edge states in finite quantum Hall graphene have previously been shown to be valley polarised for zigzag and armchair edges. Assuming that the valley isospin is also conserved at a smooth normal-superconducting (NS) interface, theoretical research has previously predicted that plateaus in the longitudinal conductance are expected to occur in the lowest Landau level of the incoming edge modes, which depends on the angle difference between the isospins entering and leaving the superconductor. In this thesis, this prediction is verified with a tight-binding simulation of six different NS junctions: for both zigzag and armchair edge nanoribbons, the superconductor can cover a single edge, two adjacent edges or two opposite edges. The theoretical prediction could be confirmed successfully, suggesting that the edge states are valley polarised along a smooth NS interface. Some deviations from the theory could be observed for the armchair edge ribbon with opposite edges when the width of the ribbon is not a multiple of three hexagons. Two consecutive widths show a complementary behaviour in the conductance such that their average corresponds to the predicted value with a remarkable robustness. The reason for this complementarity was briefly conjectured by using the special Andreev reflection in graphene and the coupling between sublattice and valley degree of freedom for zigzag edges. The parameter regimes allowing for the existence of conductance plateaus were established, confirming that the plateaus emerge for a system size much larger than the magnetic length and the superconducting coherence length, and that a smooth chemical potential, magnetic field strength and superconducting order parameter are necessary at the NS interface. The robustness of the NS edge states was furthermore investigated with three methods: a Fermi energy mismatch between the bulk and the superconductor, and random normally distributed variation in the onsite electrostatic potential and a random potential landscape. All results could confirm that intervalley scattering is the reason for deviations from the plateaus predicted by the theory.

Acknowledgements

I would like to thank Chun-Xiao for the time spent in helping me with the project, and to Anton for his guidance which made the project possible. Also, I would like to thank Antonio Manesco for his interest and suggestions, and to Michael Wimmer for taking the time for my report and defense.

Contents

Chapter 1

Introduction

1.1. Motivation and outline

Graphene is a single layer of carbon atoms which has been heavily researched over the past twenty years, notably because of its exceptional conducting properties. The presence of two nonequivalent valleys related by time reversal symmetry in its band structure is one of its unique properties. This characteristic valley degree of freedom can be treated with a two dimensional spinor in the quantum mechanical description of the particles and holes, called valley isospin. In the same way that the spin property of particles being used in solid-state devices to encode information is referred to as spintronics, exploiting the valley degree of freedom in graphene gave rise to what is now called valleytronics[1, 2]. Depending on the direction of propagation of charge carriers through graphene, all states can lie in a single valley or can be in a linear combination of states from both valleys[3]. In the presence of a strong perpendicular magnetic field on a single layer graphene nanoribbon, the propagation of charge carriers occurs exclusively at the edges of the ribbon and these edge states are valley polarised[4]. But as the conductance of such a ribbon is insensitive to the valley polarisation of these edge modes[5], the latter are difficult to identify. However, using the Andreev reflection occurring at the interface with a superconductor on the valley of incoming and outgoing states[6], Akhmerov & Beenakker (2006)[5] predicted that the angle difference Θ between the valley isospins of modes in the lowest Landau level entering and leaving the superconductor, directly depends on the longitudinal conductance G_{NS} of the NS junction in the quantum Hall regime, via the expression $G_{NS} = (1 - \cos\Theta)2e^2/h$.

In the present thesis, the predicted normal-superconducting (NS) junction conductance is computed for different edges in the tight-binding approximation. Tight-binding simulations have confirmed the validity of a comparable expression in *pn*-junctions[7, 8] and research on the Hall conductance in an NS junction is currently reviewed[9], but the prediction made by Akhmerov & Beenakker has not yet been confirmed by an experiment or a simulation. The first part of this study consists of a brief introduction to the electronic properties of graphene and the physical phenomena at work in an NS junction. Then, the tight-binding model in each regime is formulated mathematically. This is followed by a presentation of the results from the simulation. The last chapter is dedicated to investigating the effective ranges of parameters for which the model works and the robustness of the edge states at the superconducting interface.

1.2. Background

1.2.1. Electronic properties of graphene

The graphene lattice.— The carbon atoms in graphene are arranged in a honeycomb lattice. The ground state electron configuration of the carbon atom is $1s^2 2s^2 2p^2$. In a graphene monolayer, the carbon atoms are in the state corresponding to the electron configuration $1s^2 2s^1 2p_x^1 2p_y^1$. The p_z orbital is responsible for conduction in graphene through what is called π bonds[10]. The graphene lattice is non-Bravais since two neighbouring sites are inequivalent (i.e. translation of the lattice from one site to its neighbour produces a different lattice). The honeycomb structure can be decomposed into two Bravais triangular sublattices A and B which differ by a rotation of π, as demonstrated in Figure 1.2.1a. A set of lattice vectors and a basis suffice to describe the lattice geometry. Typically we choose the primitive lattice vectors of the Wigner-Seitz cell $\mathbf{a}_1 = \frac{a}{2}[3, \sqrt{3}]$ and $\mathbf{a}_2 = \frac{a}{2}[3, -\sqrt{3}]$ with basis $\{(a, 0), (2a, 0)\}$ given in Cartesian coordinates and where the lattice constant a is chosen as the carbon to carbon distance. From experiments, it approximately equals 1.42 Å[11]. The reciprocal lattice vectors can accordingly be shown to be[12] $\mathbf{b}_1 = \frac{2\pi}{3a}[1, \sqrt{3}]$ and $\mathbf{b}_2 = \frac{2\pi}{3a}[1, -\sqrt{3}]$ from which the first Brillouin zone (BZ) results as shown in Figure 1.2.1b. The corners of the BZ are denoted $\mathbf{K}$ and $\mathbf{K}'$ - three $\mathbf{K}$ and three $\mathbf{K}'$ points - of which we retain two nonequivalent ones since all the others can be obtained from the symmetry of the sublattices.

Graphene nanoribbons.— The dispersion relation of graphene gives insight in its distinctive conducting properties, in particular because of the cones touching at the Dirac points shown in Figure 1.2.1b. Instead of round shaped conduction and valence bands like most metals, the valleys in the band structure are sharp cones which touch at the $\mathbf{K}$ and $\mathbf{K}'$ points in the Brillouin Zone (BZ), called Dirac cones. These cones are locally linear and steep, as the expectation value of the group velocity $\hbar^{-1}\partial E(k)/\partial(k)$ was shown to be approximately $1.0 \cdot 10^6$ m/s theoretically[13] and experimentally [14]. Taylor expanding the dispersion relation near a Dirac cone yields a linear dispersion given by $|E| = \hbar v_F |\delta \mathbf{k}|$ where the Fermi velocity is given by $v_F = 3at/2\hbar$[4] with t the hopping potential assumed in the tight-binding model, to which we come back later. In contrast, in a graphene nanoribbon with electrons propagating in a given direction $\mathbf{k}$, the dispersion relation of infinite graphene no longer applies. Due to the finite number of conduction channels, the band structure presents only a finite number of bands as will be seen in the next paragraph. Two types of regular edges occur at the boundaries of a graphene nanoribbon. In reference to their shapes, the edges are named zigzag or armchair edges, as outlined in Figure 1.2.1a. Whether the direction of propagation is along a zigzag or an armchair edge can have important effects on the motion of charge carriers.

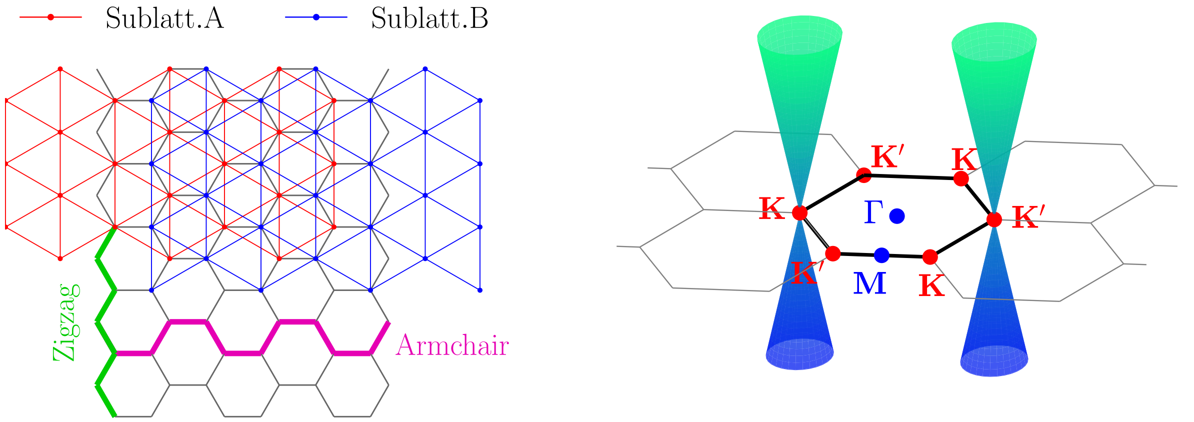

(a) Honeycomb lattice made of two triangular Bravais sublattices A and B which are not equivalent. For a finite sheet of graphene, two regular edges can occur, named zigzag and armchair edges respectively and indicated by the thick lines (made using [15, 16]).

(b) First Brillouin zone (BZ) (bold line) in the reciprocal lattice of graphene. $\mathbf{K}$ and $\mathbf{K}'$ correspond to two nonequivalent Dirac points and $\mathbf{M}$ and $\mathbf{\Gamma}$ are two other critical points. Two Dirac valleys related by time reversal symmetry from the graphene band structure are illustrated (made using [17]).

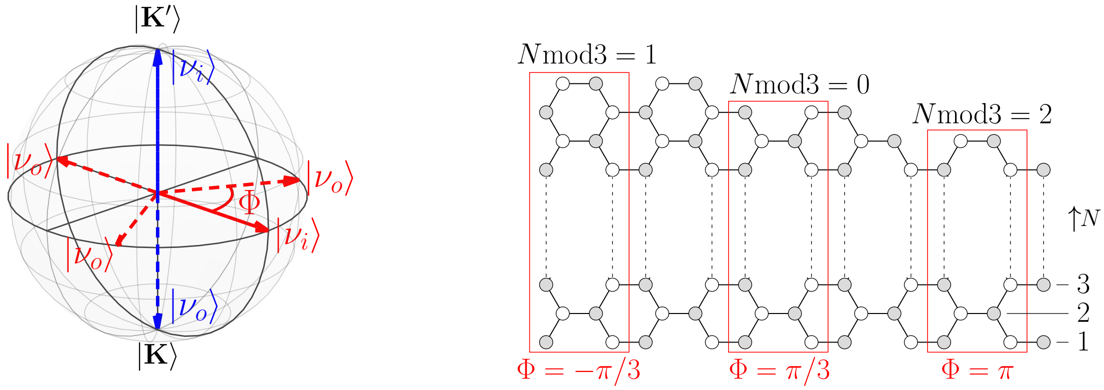

(c) States on the Bloch sphere indicating the valley isospin $\boldsymbol{\nu}$ for a zigzag edge (along z-axis, blue) and armchair edge (in xy-plane, red) graphene nanoribbon. The solid and dashed lines correspond to opposite edges. Image reproduced from [4, 8] (made using [18, 16]).

(d) Three different configurations of two opposed armchair edges in a graphene nanoribbon, with the angle of the opposite edge isospin on the Bloch sphere. Based on information from [4, 8] (made with [15, 16]).

Figure 1.2.1

Boundary conditions.— Although we will not look into the theory further, it helps to have a brief introduction to the valley isospin in graphene nanoribbons. The Schrödinger equation is no longer accurate when relativistic particles are considered. Instead, the (single particle) Dirac equation is used, given by[5]:

$$\tau_0 \otimes [v(\mathbf{p} + e\mathbf{A}) \cdot \boldsymbol{\sigma} + U]\boldsymbol{\Psi} = E\boldsymbol{\Psi}$$

where it should only be understood that the left hand side term in front of $\boldsymbol{\Psi}$ is a 4×4 matrix containing the momentum operator, the magnetic gauge, the spin degree of freedom $\boldsymbol{\sigma}$, the potential U and the valley degree of freedom $\boldsymbol{\tau}$. $\boldsymbol{\Psi}$ is therefore a 4 dimensional spinor containing the wave function amplitudes for electron and holes on each sublattice A and B, of which the ordering can be chosen conveniently in a so-called valley isotropic representation. This can be used in combination with boundary conditions of a particular graphene nanoribbon, given by[5]:

$$\mathbf{\Psi} = M\mathbf{\Psi},\ M = (\boldsymbol{\nu}\cdot\boldsymbol{\tau})\otimes(\mathbf{n}\cdot\boldsymbol{\sigma}) \tag{1.2.1}$$

which is parametrised by the valley isospin $\boldsymbol{\nu}$ and the vector $\mathbf{n}$ for which $\mathbf{n}\perp\mathbf{n_b}$, the normal vector of the boundary. In this representation, zigzag and armchair boundary conditions are fully described by[4]:

$$\begin{cases}\boldsymbol{\nu}=\pm\hat{z},\ \mathbf{n}=\hat{z} & \text{zigzag edge,}\\ \boldsymbol{\nu}\cdot\hat{z}=0,\ \mathbf{n}\cdot\hat{z}=0 & \text{armchair edge.}\end{cases}$$

The last term is verified by three different states on the Bloch sphere, with angles $\Phi = \pm\pi/3$ or $-\pi$. This different valley isospin is actually related to the geometry of a graphene armchair graphene nanoribbons. As shown in Figure 1.2.1d, there are three possible arrangements between two opposed armchair edges with different valley isospins. As we will see later, this modulus three pattern in armchair edge graphene nanoribbons arises in many electronic properties. For the zig-zag edges, there are two valley isospins verifying the boundary conditions, indicated on the Bloch sphere Figure 1.2.1c; the valley isospins of opposite edges in a nanoribbon are always perfectly opposite, in two opposed valleys, since the opposite zigzag edges are always made exclusively of atoms from the two different sublattices. Although no coupling exists between particles and holes in this system, the particle hole degree of freedom is still considered in (1.2.1) because it will become useful later when considering the superconductor. Before this, we look at the consequences of assuming the Dirac Hamiltonian and boundary conditions above on the appearance of so-called edge states.

1.2.2. Quantum Hall edge states

Placing a two-dimensional current carrying metal, say in the $\hat{x}$ direction of a Cartesian coordinates system, under a strong perpendicular magnetic field $B\hat{z}$, gives rise to a charge gradient along the $\hat{y}$ direction because of the Lorentz force. The difference in charge in turn induces an electric field against the Lorentz force. This phenomenon is known as the classical Hall effect and was first discovered by Hall in 1879[19]. Using a semi-classical derivation, the Hall resistivity ρ_{xy} can easily be shown to be proportional to the strength B of the magnetic field[12]. However, in low temperature two dimensional systems such as 2D electron gases and even stronger magnetic fields, the classical Hall effect no longer applies. Instead of a linearly increasing resistivity, one observes quantised Hall plateaus which increase in perfect integer units of h/e^2[20]. This phenomenon is called the integer quantum Hall effect (IQHE). To understand when the Hall conductance abruptly changes, one must look at the band structure of the material. When increasing the electron density in a system, the conduction bands are filled accordingly. The transition from one Hall plateau to another occurs when the Fermi energy crosses a new band, as demonstrated in Figure 1.2.2a: a new conduction channel opens up, and the conductance accordingly increases by e^2/h. The energy levels at which this transition occurs are called Landau levels: they correspond to the eigenvalues of the system Hamiltonian. For most 2D electron gases, the Hamiltonian of a free electron in a magnetic field is a good model and the Landau levels are found to be $\varepsilon_n = \omega_B(n+1/2)$, $n\in\mathbb{Z}$ [21] with $\omega_B = eB/me$ the cyclotron frequency. Note that, like in a quantum oscillator, the energy levels are evenly spaced and nonzero. However, as the Dirac equation is used, the Landau levels result in $\varepsilon_n = \mathrm{sign}(n) v_F \sqrt{2eB\hbar|n|} = \mathrm{sign}(n)\omega_D\sqrt{|n|}$, $n \in \mathbb{Z}$ with v_F the Fermi velocity[22]. Now, the Landau levels are not evenly spaced and zero is a Landau level. There exists another even stronger peculiarity in graphene: it has its own version of the quantum Hall effect, often called anomalous because of its unique half-integer quantisation[23] given by $\sigma_{xy} = 4e^2/h \cdot (n + 1/2)$ where n is the index the Landau level, first shown experimentally in 2005[14] (cf. Figure 1.2.2c). The reason that the Hall conductivity increases in steps of $4e^2/h$ and not of $1e^2/h$ is roughly because of two degrees of freedom present in graphene: two spin degrees of freedom and two valley degrees of freedom. This can immediately be seen in the band structure of a graphene GNR (here armchair edge) in Figure 1.2.2c: the lowest Landau level has only two bands, and the higher ones increase in steps of four bands.

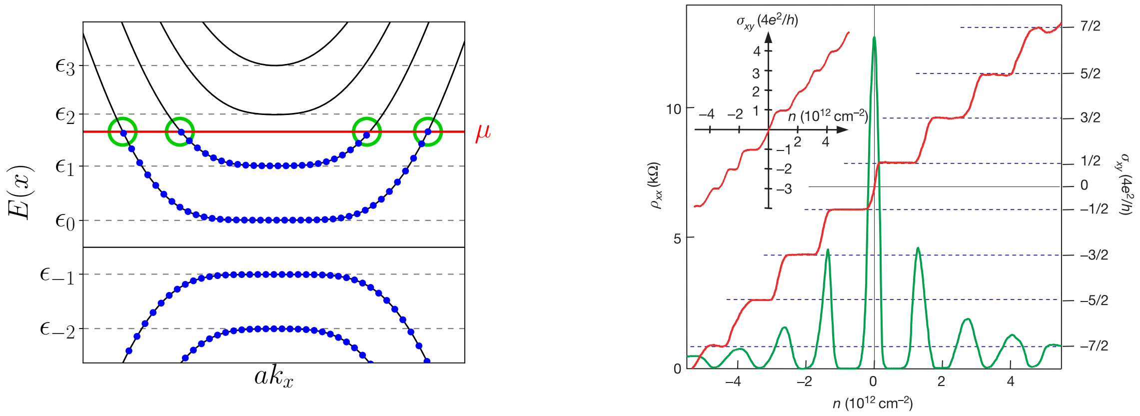

(a) Typical band structure appearance of a Hall bar based on [24]. The Landau levels are indicated by dashed lines. Blue dots represent electrons in bands under the Fermi level (red line) and green circles sho the edge-modes.

(b) Measurements of the Hall conductivity σ_{xy} in graphene and longitudinal resistivity ρ_{xx} as a function of the electron concentration, in a magnetic field $B = 14$ T and $T = 4$ K. Retrieved from Novoselov et al. (2005)[14].

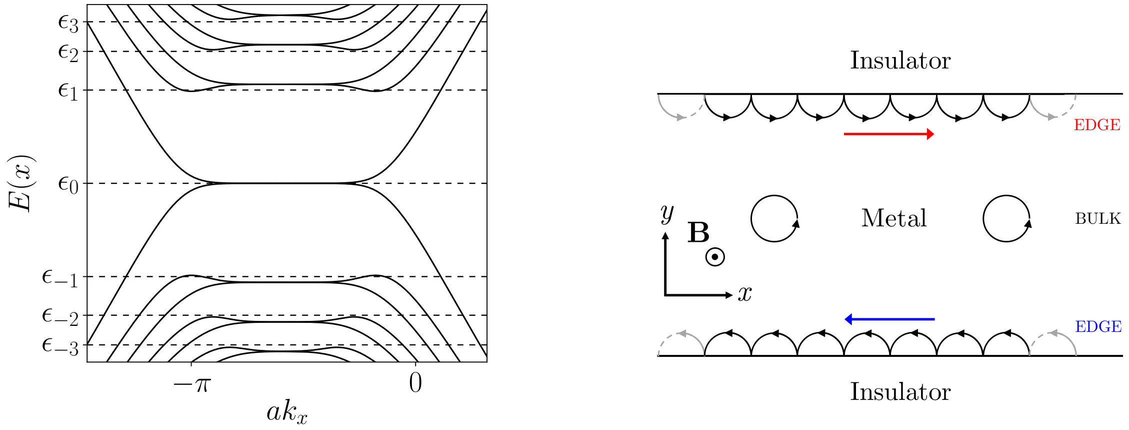

(c) Band structure of an armchair edge graphene nanoribbon in the quantum Hall regime for a strong (arbitrary) magnetic field. The Landau levels $\epsilon_n \propto \sqrt{|n|}$ are indicated with dashed lines.

(d) Semi-classical representation of edge states in a Hall bar for a strong magnetic field (pointing out of the paper). The edges are chiral; the top (bottom) edge state moves to the right (left) and the bulk carries no current.

Figure 1.2.2

Note that only the longitudinal conductance is relevant in this study and not the Hall conductance. The latter is measured accross the GNR (often denoted with the subscript xy) whereas the former is measured at both ends (subscript xx). We still refer to it as the quantum Hall regime in our system because the quantum Hall effect is at the heart of the edge-states we are interested in. Figure 1.2.2a shows that the expectation value of the velocity, defined by the derivative of the band structure $v_n = \hbar^{-1}\partial\varepsilon_n(k_x)/\partial x$, is negative, null and positive in the left, middle, and right parts respectively. The nonzero velocity modes correspond to electron states at the edges of the GNR whereas the zero velocity modes are the electrons in the bulk, which are on average immobile. Figure 1.2.2d shows a semi-classical visualisation of these edge states. The application of a magnetic field on a lattice causes electrons to move in cyclotron orbits. Thus, electrons in the bulk will mostly stay at the same location and there will be no current. Close to the edges however, electrons must collide with the insulating boundaries instead of moving in orbitals. As a result, they skip along the edges and induce a current, in opposite directions at the opposite edges: this is why they are called chiral.

1.2.3. Andreev reflection at a superconducting interface

Superconductivity is the phenomenon by which a material carries current without resistance. When first observed in 1911[25], superconductivity would arise in some materials under a critical temperature T_c. The microscopic theory of superconductivity was proposed by Bardeen, Cooper, and Schrieffer in 1957, known as BCS theory[26]. Charge carriers in a superconductor are called Cooper pairs. They consist of a pair of two electrons bounded by a weak Coulomb interaction and, in the current case of S-wave superconductors, their total spin is 0 as the two electrons in the cooper pair have opposite spins. At energies above what is called the superconducting gap Δ_0, no Cooper pairs are able to form anymore. A brief introduction to the concept of superconductivity can be found in [27] and a full introduction in [28]. In this thesis we only consider the BCS theory of superconductivity, and in particular, Andreev reflection, which we introduce underneath. A single sheet of graphene is intrinsically a poor superconductor[6] but superconductivity can be induced artificially by a superconducting contact[29, 30], or as discovered recently, at room temperature by putting a second graphene layer on top rotated at a ”magical” angle[31].

Andreev reflection is a special feature arising at the interface between a normal metal and a superconductor discovered in 1964[32]. In the semi-classical representation, when an electron with charge $-e$ with subgap energy incident from the normal side of the interface hits the superconductor, it is absorbed into the superconductor and a cooper pair with charge $-2e$ in the ground state is formed. In order to conserve charge, a hole with charge e is reflected back. Effectively, this reflection transforms an electron into a hole, and vice versa. In the description of Andreev reflection, one assumes no momentum is lost at the interface. This is valid if the superconducting gap is much smaller than the chemical potential of the normal metal[33]. The hole follows the same trajectory as the electron, but in reverse which is called retroreflection, due to conservation of momentum. The hole must have a negative effective mass and therefore a negative velocity relatively to the incident electron. For a superconducting coherence length $\xi = \hbar v_F/\Delta$ much smaller than the Fermi wavelength, graphene presents an exclusive kind of Andreev reflection called specular Andreev reflection[6]: an electron with momentum $\mathbf{p}_e = \hbar\mathbf{K}$ is converted to a hole with momentum of the opposite valley $\mathbf{p}_h = \hbar\mathbf{K}' = -\hbar\mathbf{K}$. This reflection is displayed in Figures 1.2.3a.

In a graphene nanoribbon under a strong magnetic field, edge states approaching the superconductor can be Andreev reflected along the interface as illustrated in Figure 1.2.3b. Along the NS interface, the propagating modes are mixed electron and hole states because of Andreev reflection. Because of the valley isotropic boundary condition, the propagating modes along the NS interface are valley degenerate. One can roughly expect that the valley polarisation of the incoming/outgoing edge states affects the conductance (which we will not go further into), predicted based on the conservation of valley isospin[5]:

$$G_{NS} = (1 - \cos\Theta)e^2/h.$$

From Blonder-Tinkham-Klapwijk (BTK) theory[34], an intuitive result can be obtained[5]: if the state leaving the superconductor is a hole with probability of one, then all the incoming edge states were transmitted as supercurrent into the superconductor. If an electron is reflected back with probability of one, then no current entered the superconductor. In general[5]:

$$G_{NS} = \frac{e^2}{h}(1 - T_{ee} + T_{he}) \tag{1.2.2}$$

where T_{ee} is the probability that an electron is reflected back along the opposite edge and T_{he} the probability that an incoming electron returns back as a hole. The latter equation will be used later on in order to verify the former one.

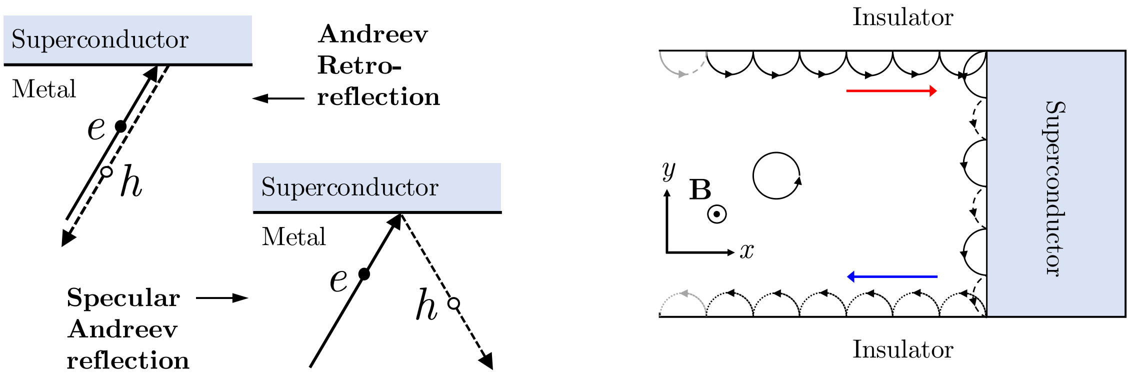

(a) Classical representation of two types of Andreev reflections at a metal-superconductor interface. Specular Andreev reflection is a special case occurring at the interface of superconducting graphene in which the electron and hole lie in opposite valleys. Images reproduced from [6].

(b) Classical representation of Andreev reflection at a superconducting interface in the quantum Hall regime of a nanoribbon. The incoming edge state (solid lines orbits) is Andreev reflected along the interface (solid/dashed lines). The outgoing edge state can be a superposition of electron and hole (dotted lines orbits).

Figure 1.2.3

Chapter 2

Tight-binding descriptions of graphene

When considering large systems of particles on a lattice, assuming the wave functions of electrons to be a linear combination of the atomic orbitals (LCAO) can be convenient. The proposed variational solution minimises the energy[12] and results in what is known as a tight-binding model. Although the electron-hole symmetry which follows is an idealised version of graphene, the nearest neighbour (NN) tight-binding model is a good approximation for the electronic band structure of graphene[35] and is computationally efficient. In the current chapter, we formulate the tight-binding model of graphene in three regimes: normal, quantum Hall and superconducting. We also describe the geometry of the graphene lattice and its main electronic properties derived from the model. The resulting Hamiltonians will be used in the numerical implementation of the junctions in the next chapter.

2.1. Tight-binding description of normal graphene

In this section, the tight-binding Hamiltonian and dispersion relation of infinite normal graphene is derived using two different methods. The first one uses a linear combination of atomic orbitals as introduced before, while the second method, which is more compact, uses second quantisation formalism.

2.1.1. Linear combination of atomic orbitals

The single-electron Hamiltonian on a lattice is given by[12]:

$$\hat{H} = \frac{\hat{\mathbf{p}}^2}{2m} + \sum_{\mathbf{R}_j} \hat{V}(\mathbf{r} - \mathbf{R}_j) \tag{2.1.1}$$

where $\hat{\mathbf{p}}^2/\hbar^2 = \nabla^2$ is the Laplacian operator with respect to the electron position $\mathbf{r}$ and the summation runs over all lattice sites. The electrostatic potential operator $\hat{V}$ has the same periodicity as the lattice since it is the atomic potential. In our case, the lattice is bipartite so the following modification is made to the Hamiltonian:

$$\hat{H} = \frac{\hat{\mathbf{p}}^2}{2m} + \sum_{\mathbf{R}_j} \Big(\hat{V}(\mathbf{r} - \mathbf{r}_1 - \mathbf{R}_j) + \hat{V}(\mathbf{r} - \mathbf{r}_2 - \mathbf{R}_j) \Big) \tag{2.1.2}$$

where the summation runs over all unit-cells, and $\mathbf{r}_1$ and $\mathbf{r}_2$ indicate the positions of the two carbons relative to $\mathbf{R}_j$, some reference coordinate in the unit-cell. For a nearest neighbour approximation, the orbital wave functions of the atomic Hamiltonian must be well localised[36] at the range of the lattice constant and the positions of atoms are assumed to be fixed so that the wave functions of electrons can be treated separately from the atomic wave functions (Born-Oppenheimer approximation [37]).

Our next step is assuming a certain wave function for the electrons [12]:

$$\psi_{\mathbf{k}}(\mathbf{r}) = \sum_{\mathbf{R}_j} e^{i\mathbf{k}\cdot\mathbf{R}_j}\phi(\mathbf{r}-\mathbf{R}_j) \tag{2.1.3}$$

with $\mathbf{R}_j$ the set of all points in one of the sublattices such that $\mathbf{R}_j = n_1\mathbf{a}_1 + n_2\mathbf{a_2}$ for all pairs $(n_1, n_2) \in \mathbb{N}^2$ and with $\phi(\mathbf{r})$ the atomic p$_z$ orbitals. This solution is called a Wannier function and can be easily verified to satisfy the Bloch theorem[36]. As the latter only applies to Bravais lattices, the orbitals for a bipartite lattice are written as a linear combination of orbitals from both sublattices:

$$\phi(\mathbf{r}) = c_A\phi_A(\mathbf{r}) + c_B\phi_B(\mathbf{r}). \tag{2.1.4}$$

We now substitute (2.1.3) and (2.1.4) into the time independent Schrödinger equation:

$$E(\mathbf{k})\psi_{\mathbf{k}} = \hat{H}\psi_{\mathbf{k}},$$

The two parameters c_A and c_B can be found by projecting $\psi_{\mathbf{k}}$ on the two states and solving the time independent Schrödinger equation:

$$\begin{cases} \langle\phi_A(\mathbf{r})| E(\mathbf{k}) |\psi(\mathbf{r})\rangle = \langle\phi_A(\mathbf{r})| \hat{H}(\mathbf{k}) |\psi(\mathbf{r})\rangle \\ \langle\phi_B(\mathbf{r})| E(\mathbf{k}) |\psi(\mathbf{r})\rangle = \langle\phi_B(\mathbf{r})| \hat{H}(\mathbf{k}) |\psi(\mathbf{r})\rangle \end{cases} \Rightarrow \begin{cases} E(\mathbf{k}) \langle\phi_A(\mathbf{r})|\psi(\mathbf{r})\rangle = \langle\phi_A(\mathbf{r})| \hat{H}(\mathbf{k}) |\psi(\mathbf{r})\rangle \\ E(\mathbf{k}) \langle\phi_B(\mathbf{r})|\psi(\mathbf{r})\rangle = \langle\phi_B(\mathbf{r})| \hat{H}(\mathbf{k}) |\psi(\mathbf{r})\rangle \end{cases} \tag{2.1.5}$$

Simplifying the left-hand side for ϕ_A gives:

$$\begin{aligned} \langle\phi_A(\mathbf{r})|\psi(\mathbf{r})\rangle &= \langle\phi_A| \sum_{\mathbf{R}_j} \big(c_A\phi_A(\mathbf{r}-\mathbf{R}_j)e^{i\mathbf{k}\cdot\mathbf{R}_j} + c_B\phi_B(\mathbf{r}-\mathbf{R}_j)e^{i\mathbf{k}\cdot\mathbf{R}_j}\big)\rangle \\ &= \sum_{\mathbf{R}_j} \big(c_A \langle\phi_A(\mathbf{r})|\phi_A(\mathbf{r}-\mathbf{R}_j)\rangle e^{i\mathbf{k}\cdot\mathbf{R}_j} + c_B \langle\phi_A(\mathbf{r})|\phi_B(\mathbf{r}-\mathbf{R}_j)\rangle e^{i\mathbf{k}\cdot\mathbf{R}_j}\big) \\ &= c_A \langle\phi_A(\mathbf{r})|\phi_A(\mathbf{r})\rangle + c_B \langle\phi_A(\mathbf{r})|\phi_B(\mathbf{r})\rangle (1 + e^{-i\mathbf{k}\cdot\mathbf{a}_1} + e^{-i\mathbf{k}\cdot\mathbf{a}_2}) \\ &= c_A + c_B s(1 + e^{-i\mathbf{k}\cdot\mathbf{a}_1} + e^{-i\mathbf{k}\cdot\mathbf{a}_2}) \end{aligned}$$

where in the third rule, only the nearest neighbour wave-functions were considered in the sum, and all the other overlap integrals were assumed to be zero. In the last rule, the overlap integral was renamed to $s \equiv \langle\phi_A(\mathbf{r})|\phi_B(\mathbf{r})\rangle$. Repeating the above for ϕ_B yields:

$$\langle\phi_B(\mathbf{r})|\psi(\mathbf{r})\rangle = c_B + c_A s^*(1 + e^{-i\mathbf{k}\cdot\mathbf{a}_1} + e^{-i\mathbf{k}\cdot\mathbf{a}_2})$$

where we assume that $s \in \mathbb{R}$ so that $s^* = s$.

The right-hand side from equation (2.1.5) can also be simplified. For this purpose, we rewrite the term $\hat{H}\phi_A$ in the following way:

$$\begin{aligned}
\hat{H}\phi_A(\mathbf{r}) &= \frac{\hat{\mathbf{p}}^2}{2m}\phi_A(\mathbf{r}) + \sum_{\mathbf{R}_j}\left(\hat{V}(\mathbf{r}-\mathbf{r}_1-\mathbf{R}_j) + \hat{V}(\mathbf{r}-\mathbf{r}_2-\mathbf{R}_j)\right)\phi_A(\mathbf{r}) \\
&= \varepsilon_A\phi_A(\mathbf{r}) + \left(\sum_{\mathbf{R}_j\neq\mathbf{r}}\left(\hat{V}(\mathbf{r}-\mathbf{r}_1-\mathbf{R}_j) + \hat{V}(\mathbf{r}-\mathbf{r}_2-\mathbf{R}_j)\right) + \hat{V}(-\mathbf{r}_2)\right)\phi_A(\mathbf{r}) \\
&= \varepsilon_A\phi_A(\mathbf{r}) + \hat{U}_A\phi_A(\mathbf{r}), \qquad (2.1.6)
\end{aligned}$$

where the potential felt due to the surrounding atoms is written as $\hat{U}_A$. Similarly for ϕ_B:

$$\hat{H}\phi_B(\mathbf{r}) = \varepsilon_B\phi_B(\mathbf{r}) + \hat{U}_B\phi_B(\mathbf{r}). \qquad (2.1.7)$$

We are free to set the zero point energy $\varepsilon_A = \varepsilon_B = 0$. It follows that:

$$\langle\phi_A(\mathbf{r})|\,\hat{H}\,|\psi(\mathbf{r})\rangle = \sum_{\mathbf{R}_j}\left(c_A(\mathbf{r}-\mathbf{R}_j)e^{i\mathbf{k}\cdot\mathbf{R}_j}\langle\phi_A|\,\hat{H}\,|\phi_A\rangle + c_B(\mathbf{r}-\mathbf{R}_j)e^{i\mathbf{k}\cdot\mathbf{R}_j}\langle\phi_A|\,\hat{H}\,|\phi_B\rangle\right).$$

Substituting (2.1.6) and (2.1.7) yields:

$$\begin{aligned}
\langle\phi_A(\mathbf{r})|\,\hat{H}\,|\psi(\mathbf{r})\rangle &= \sum_{\mathbf{R}_j}\left(c_A\langle\phi_A|\hat{U}_A|\phi_A\rangle e^{i\mathbf{k}\cdot\mathbf{R}_j} + c_B\langle\phi_A|\hat{U}_B|\phi_B\rangle e^{i\mathbf{k}\cdot\mathbf{R}_j}\right) \\
&= c_A\langle\phi_A|\hat{U}_A|\phi_A\rangle + c_B\langle\phi_A|\hat{U}_B|\phi_B\rangle(1+e^{-i\mathbf{k}\cdot\mathbf{a}_1}+e^{-i\mathbf{k}\cdot\mathbf{a}_2}) \\
&\equiv c_B t(1+e^{-i\mathbf{k}\cdot\mathbf{a}_1}+e^{-i\mathbf{k}\cdot\mathbf{a}_2}).
\end{aligned}$$

where only nearest neighbour orbitals were included in the sum, and where $t \in \mathbb{R}$ is assumed and referred to as the hopping potential. Similarly for ϕ_B we have:

$$\langle\phi_B(\mathbf{r})|\,\hat{H}\,|\psi(\mathbf{r})\rangle = c_A t(1+e^{-i\mathbf{k}\cdot\mathbf{a}_1}+e^{-i\mathbf{k}\cdot\mathbf{a}_2}).$$

Now the equations (2.1.5) are reduced to the system:

$$\begin{pmatrix} E(\mathbf{k}) & (1+e^{-i\mathbf{k}\cdot\mathbf{a}_1}+e^{-i\mathbf{k}\cdot\mathbf{a}_2})(sE(\mathbf{k})-t) \\ (1+e^{i\mathbf{k}\cdot\mathbf{a}_1}+e^{i\mathbf{k}\cdot\mathbf{a}_2})(sE(\mathbf{k})-t) & E(\mathbf{k}) \end{pmatrix}\begin{pmatrix} c_A \\ c_B \end{pmatrix} = \begin{pmatrix} 0 \\ 0 \end{pmatrix}.$$

Assuming that the orbitals from neighbouring sites are orthogonal (i.e. $s = \langle\phi_A(\mathbf{r})|\phi_B(\mathbf{r})\rangle = 0$), diagonalising the matrix yields the tight-binding dispersion relation $E(\mathbf{k}) = \pm t|(1 + e^{-i\mathbf{k}\cdot\mathbf{a}_1} + e^{-i\mathbf{k}\cdot\mathbf{a}_2})|$. In the next paragraph, this expression is derived in a different formalism, but with the same principles, and will be simplified and graphed.

2.1.2. Second quantisation Hamiltonian

For more complicated systems, it is particularly convenient to work with a different representation: instead of characterising each quantum state with a superposition of wave functions, it is simply denoted by the number of particles in that particular state $|n_1, n_2, ...\rangle$ with n_i the occupation of state $|\psi_i\rangle$. Then, the state of an electron on each atomic site can be denoted as such. Applying the so-called creation operator $\hat{c}_i^\dagger$ on $|\psi_i\rangle$ increases the number of particles in that state by one. The reverse applies for the annihilation operator $\hat{c}_i$. For further lecture, we refer to Appendix A for a short summary and [38] for a full introduction to second quantisation formalism. The definition of creation and annihilation operators must obey the Pauli exclusion principle. This is remedied by their definition, and seen in the (anti) commutation relations[38]:

$$\begin{cases} \hat{c}_i \left|n_1, ..., n_i, ...\right\rangle = \sqrt{n_i}\zeta^{s_i} \left|n_1, ..., n_i - 1, ...\right\rangle & \text{annihilation} \\ \hat{c}_i^\dagger \left|n_1, ..., n_i, ...\right\rangle = \sqrt{n_i + 1}\zeta^{s_i} \left|n_1, ..., n_i + 1, ...\right\rangle & \text{creation} \\ [\hat{c}_i^\dagger, \hat{c}_j^\dagger]_\zeta = 0,\ [\hat{c}_i, \hat{c}_j]_\zeta = 0,\ [\hat{c}_i, \hat{c}_j^\dagger] = \delta_{ij} & \text{(anti-)commutator relations} \end{cases} \tag{2.1.8}$$

where ζ was introduced a shorthand to characterise Fermions ($\zeta = -1$) and Bosons ($\zeta = 1$) in the same definition. Also, $[\hat{A}, \hat{B}]_\zeta = \hat{A}\hat{B} - \zeta\hat{B}\hat{A}$ is the (anti) commutator for $\zeta = 1$ ($\zeta = -1$). Observe that when applying $\hat{c}_i\hat{c}_i^\dagger$ onto an arbitrary state $\left|\psi\right\rangle$, one obtains $\hat{c}_i\hat{c}_i^\dagger \left|\psi\right\rangle = n_i \left|\psi\right\rangle$ with n_i the number of electrons in state i. One last but useful result from second quantisation is the transformation of creation and annihilation operators from real to reciprocal space:

$$\hat{c}_j = \frac{1}{\sqrt{N}} \sum_{\mathbf{k}\in\mathrm{BZ}} e^{i\mathbf{k}\cdot\mathbf{R}_j} \hat{c}_{\mathbf{k}} \quad \text{and} \quad \hat{c}_{\mathbf{k}} = \frac{1}{\sqrt{N}} \sum_j e^{i\mathbf{k}\cdot\mathbf{R}_j} \hat{c}_j. \tag{2.1.9}$$

In this formalism, the tight-binding Hamiltonian can be written in terms of annihilation of an electron (or hole) at one site, and creation at another site. For example, when an electron tunnels from a site l to a site j, the corresponding hopping Hamiltonian is $-t(\hat{c}_l^\dagger\hat{c}_j + \hat{b}_c^\dagger\hat{c}_l)$ where creation/annihilation operators for both sublattices were introduced. The second term is often abbreviated by h.c. for Hermitian conjugate. The tight-binding Hamiltonian in second quantisation is given by:

$$\hat{H}_{\mathrm{G}} = -t \sum_{\langle l,j\rangle,\sigma} (\hat{c}_{l\sigma}^\dagger \hat{c}_{j\sigma} + \text{h.c.}) = -t \sum_{\mathbf{R},\boldsymbol{\delta},\sigma} (\hat{c}_{\mathbf{R},\sigma}^\dagger \hat{c}_{\mathbf{R}+\boldsymbol{\delta},\sigma} + \text{h.c.}) \tag{2.1.10}$$

where the vectors $\boldsymbol{\delta}$ correspond to the difference in position between an A atom and its nearest neighbours, given by:

$$\boldsymbol{\delta}_1 = \frac{a}{2}[1, \sqrt{3}], \boldsymbol{\delta}_2 = \frac{a}{2}[1, -\sqrt{3}], \boldsymbol{\delta}_3 = \frac{a}{2}[-2, 0].$$

The hopping potential t is often taken 2.7 or 2.8 eV[35, 11] depending on the literature. Like in the LCAO derivation, the Hamiltonian is sought to be diagonalised in order to obtain the dispersion relation of graphene. Therefore, the Hamiltonian is first considered in **k**-space where we use the transformations from equation (2.1.9) and obtain:

$$\begin{aligned} \hat{H}_G &= -\frac{t}{N} \sum_{\mathbf{R},\boldsymbol{\delta}} \sum_{\mathbf{k},\mathbf{k}'} (\hat{a}_{\mathbf{k}}^\dagger \hat{b}_{\mathbf{k}'} e^{i\mathbf{k}'\cdot\boldsymbol{\delta}} e^{i\mathbf{R}\cdot(\mathbf{k}-\mathbf{k}')} + \text{h.c.}) \\ &= -t \sum_{\boldsymbol{\delta}} \sum_{\mathbf{k},\mathbf{k}'} (\hat{a}_{\mathbf{k}}^\dagger \hat{b}_{\mathbf{k}'} e^{i\mathbf{k}'\cdot\boldsymbol{\delta}} \left(\frac{1}{N} \sum_{\mathbf{R}} e^{i\mathbf{R}\cdot(\mathbf{k}-\mathbf{k}')} \right) + \text{h.c.}) \\ &= -t \sum_{\boldsymbol{\delta}} \sum_{\mathbf{k},\mathbf{k}'} (\hat{a}_{\mathbf{k}}^\dagger \hat{b}_{\mathbf{k}'} e^{i\mathbf{k}'\cdot\boldsymbol{\delta}} \delta_{\mathbf{k},\mathbf{k}'} + \text{h.c.}) \\ &= -t \sum_{\boldsymbol{\delta},\mathbf{k}} (\hat{a}_{\mathbf{k}}^\dagger \hat{b}_{\mathbf{k}} e^{i\mathbf{k}\cdot\boldsymbol{\delta}} + \text{h.c.}) \end{aligned}$$

where the spin degree of freedom was omitted for this particular derivation. If one introduces $\hat{\Psi}_{\mathbf{k}} = (\hat{a}_{\mathbf{k}}, \hat{b}_{\mathbf{k}})^{\intercal}$, the latter may be rewritten into:

$$\hat{H}_G = \sum_{\mathbf{k}} \hat{\Psi}^{\dagger}_{\mathbf{k}} h(\mathbf{k}) \hat{\Psi}_{\mathbf{k}} \quad \text{with} \quad h(\mathbf{k}) = \begin{pmatrix} 0 & f(\mathbf{k}) \\ f^*(\mathbf{k}) & 0 \end{pmatrix} \tag{2.1.11}$$

where $f(\mathbf{k}) = -t\sum_{\boldsymbol{\delta}} e^{i\mathbf{k}\cdot\boldsymbol{\delta}} = -t(e^{-ik_x a} + 2e^{ik_x a/2}\cos(k_y a\sqrt{3}/2))$. The matrix h is called the Bloch Hamiltonian[39] and is diagonalisable since it is Hermitian. It follows that the eigenvalues of h yield the energy dispersion relation:

$$E_{\pm}(\mathbf{k}) = \pm|f(\mathbf{k})| = \pm t\sqrt{3 + 2\cos(\sqrt{3}k_y a) + 4\cos(\sqrt{3}k_y a/2)\cos(\sqrt{3}k_x a/2)} \tag{2.1.12}$$

which is shown with the BZ in Figure 2.1.1a. Due to their high degree of symmetry, the critical points of the BZ can help remove the redundancy in the dispersion relation as shown in Figure 2.1.1b. Conventionally, Γ and M are other critical points[40] of the BZ corresponding to the center of the BZ and of an edge respectively.

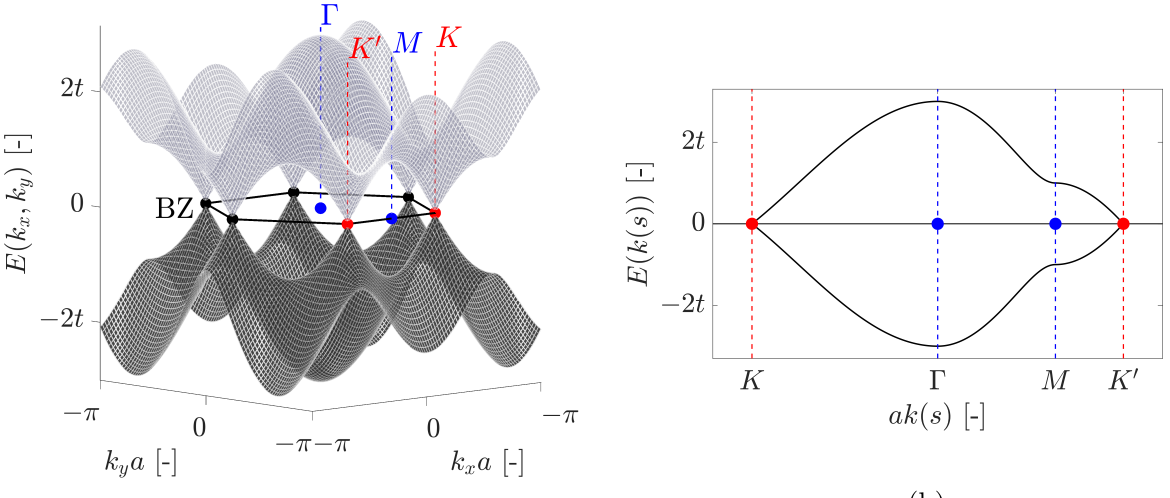

(a) (b)

Figure 2.1.1: Left: Nearest neighbour tight-binding (NNTB) energy dispersion relation of graphene plotted onto the Brillouin zone (BZ). The bottom (dark) is the valence band and the top (light) is the conduction band. Right: NNTB Dispersion relation along the path parametrized by s linking the critical points in the BZ. The Fermi energy was set to 0. Made using [17].

2.2. Tight-binding description of quantum Hall graphene

In the presence of a magnetic field $\mathbf{B} = \nabla \times \mathbf{A}(\mathbf{r})$ perpendicular to the lattice, the hopping potential will gain a phase, called the Peierls phase ϕ_{lj}, introduced in the substitution $t_{lj} \rightarrow t_{lj}e^{i\phi_{lj}}$. Without this phase, the wave function satisfying the Schrödinger (or Dirac) equation for the changed Hamiltonian $\hat{H} = \frac{1}{2m}(\mathbf{p} + e\mathbf{A})^2 + \hat{V}(\mathbf{r})$ does not obey the Bloch theorem anymore[41]. The Peierls substitution ensures the electron wave function acquires the right phase over a plaquette. Upon tunnelling from a site l to a site j, the acquired phase is[42]:

$$\phi_{lj} = \frac{2\pi e}{\hbar c} \int_{\mathbf{r}_l}^{\mathbf{r}_j} \mathbf{A} \cdot \mathbf{d}\ell \tag{2.2.13}$$

which integrates the vector potential $\mathbf{A}$ over the path from site l to site j. A homogeneous magnetic field $\mathbf{B} = B_0\hat{\mathbf{z}}$ is verified by the Landau gauges $\mathbf{A} = B_0 x\hat{\mathbf{y}}$ and $\mathbf{A} = -B_0 y\hat{\mathbf{x}}$. If the system is translation invariant in the $\hat{\mathbf{x}}$ ($\hat{\mathbf{y}}$) direction, the Landau gauge is chosen in the $\hat{\mathbf{x}}$ ($\hat{\mathbf{y}}$) direction. It follow that the tight binding Hamiltonian (2.1.10) is changed into[43]:

$$\hat{H} = -t \sum_{\langle l,j\rangle,\sigma} (\hat{c}^\dagger_{l\sigma}\hat{c}_{j\sigma}e^{i\theta_{lj}} + \text{h.c.}) = -t \sum_{\mathbf{R},\boldsymbol{\delta}} (\hat{c}^\dagger_{\mathbf{R},\sigma}\hat{c}_{\mathbf{R}+\boldsymbol{\delta},\sigma}e^{i\theta_{\mathbf{R}\mathbf{R}+\boldsymbol{\delta}}} + \text{h.c.}) \tag{2.2.14}$$

Assuming $\mathbf{A} = B_0 y\hat{\mathbf{x}}$ numerical integration of the vector potential along the hopping path (2.2.13) is performed with the midpoint integration method:

$$\phi_{lj} = 2\pi\frac{B_0}{\phi_0}\left(\frac{1}{2}(x_l - x_j)(y_l + y_j)\right) = 2\pi\frac{\phi}{\phi_0}\frac{1}{A}\left(\frac{1}{2}(x_l - x_j)(y_l + y_j)\right)$$

with $\phi_0 = hc/e$ the magnetic flux quantum, ϕ the magnetic flux through one hexagonal plaquette, and $A = 3\sqrt{3}a^2/2$ the area of a plaquette. (x_l, y_l) and (x_j, y_j) are the Cartesian coordinates of sites l and j respectively. For consistency with the Hamiltonian described in the next section, we wish to write the Hamiltonian between two single sites in reduced form using the basis $\mathbf{\Psi}_i = (\hat{c}_{i\uparrow}, \hat{c}_{i\downarrow}, \hat{c}^\dagger_{i\downarrow}, -\hat{c}^\dagger_{i\uparrow})$, which is done using the anti-commutation relations from equation (2.1.8):

$$\begin{aligned}
\hat{H}_{lj} &= -te^{i\phi_{lj}}(\hat{c}^\dagger_{l\uparrow}\hat{c}_{j\uparrow} + \hat{c}^\dagger_{l\downarrow}\hat{c}_{j\downarrow}) - te^{-i\phi_{lj}}(\hat{c}^\dagger_{j\uparrow}\hat{c}_{l\uparrow} + \hat{c}^\dagger_{j\downarrow}\hat{c}_{l\downarrow}) \\
&= -te^{i\phi_{lj}}(\hat{c}^\dagger_{l\uparrow}\hat{c}_{j\uparrow} + \hat{c}^\dagger_{l\downarrow}\hat{c}_{j\downarrow}) + te^{-i\phi_{lj}}(\hat{c}_{l\uparrow}\hat{c}^\dagger_{j\uparrow} + \hat{c}_{l\downarrow}\hat{c}^\dagger_{j\downarrow}) \\
&= (\mathbf{\Psi}^\dagger_l)^\intercal \begin{pmatrix} -te^{i\phi_{lj}} & \circ & \circ & \circ \\ \circ & -te^{i\phi_{lj}} & \circ & \circ \\ \circ & \circ & te^{-i\phi_{lj}} & \circ \\ \circ & \circ & \circ & te^{-i\phi_{lj}} \end{pmatrix} \mathbf{\Psi}_j \\
&= (\mathbf{\Psi}^\dagger_l)^\intercal \begin{pmatrix} (-t\cos\phi_{lj} - it\sin\phi_{lj})\cdot\sigma_0 & \circ\cdot\sigma_0 \\ \circ\cdot\sigma_0 & (-t\cos\phi_{lj} + it\sin\phi_{lj})\cdot\sigma_0 \end{pmatrix} \mathbf{\Psi}_j \\
&= -t(\mathbf{\Psi}^\dagger_l)^\intercal[\cos\phi_{lj}\tau_z + i\sin\phi_{lj}\tau_0] \otimes \sigma_0\mathbf{\Psi}_j
\end{aligned}$$

where the Kronecker[44] product $\otimes$ was used to abbreviate the reduced Hamiltonian. σ_0 denotes the identity matrix corresponding to the spin degree of freedom and in general $\sigma_x, \sigma_y, \sigma_z$ denote the Pauli spin matrices. The particle-hole degree of freedom is expressed by the set of Pauli matrices denoted by τ_i. As anticipated physically, the Hamiltonian acts identically on both spin states (i.e. there is no spin coupling).

2.3. Tight-binding description of superconducting graphene

The Hamiltonian for an s-wave superconducting lattice with N sites contains a term Δ which couples electrons to holes in the following way[45]:

$$\begin{aligned}\hat{H} &= \sum_{j=1}^{N} \left(\Delta \hat{c}^{\dagger}_{j\uparrow} \hat{c}^{\dagger}_{j\downarrow} + \Delta^{*} \hat{c}_{j\downarrow} \hat{c}_{j\uparrow} \right) \\ &= \sum_{j=1}^{N} \left(\frac{\Delta}{2} \hat{c}^{\dagger}_{j\uparrow} \hat{c}^{\dagger}_{j\downarrow} - \frac{\Delta}{2} \hat{c}^{\dagger}_{j\downarrow} \hat{c}^{\dagger}_{j\uparrow} + \frac{\Delta^{*}}{2} \hat{c}_{j\downarrow} \hat{c}_{j\uparrow} - \frac{\Delta^{*}}{2} \hat{c}_{j\uparrow} \hat{c}_{j\downarrow} \right)\end{aligned}$$

where the fermionic commutation relations (2.1.8) were used. Δ is called the superconducting pairing potential or superconducting order parameter, generally written $\Delta = \Delta_0 e^{i\phi}$ where Δ_0 is the superconducting gap. This term should be seen as the potential which creates or destroys a Cooper pair with total spin 0. For a convenient representation of the Hamiltonian, the choice of the Nambu basis is $\mathbf{\Psi} = (\hat{c}_{1\uparrow}, \hat{c}_{1\downarrow}, \hat{c}_{2\uparrow}, \hat{c}_{2\downarrow}, ..., \hat{c}_{N\downarrow}, \hat{c}^{\dagger}_{1\downarrow}, -\hat{c}^{\dagger}_{1\uparrow}, \hat{c}^{\dagger}_{2\downarrow}, -\hat{c}^{\dagger}_{2\uparrow}, ..., -\hat{c}^{\dagger}_{N\uparrow})^{\intercal}$, which allows for rewriting the latter into matrix form, called the Bogoliubov-de Gennes Hamiltonian:

$$\begin{aligned}\hat{H}_{BdG} &= \frac{1}{2} (\mathbf{\Psi}^{\dagger})^{\intercal} \begin{pmatrix} H_e & \mathbf{\Delta} \\ \mathbf{\Delta}^{*} & H_h \end{pmatrix} \mathbf{\Psi} = \frac{1}{2} (\mathbf{\Psi}^{\dagger})^{\intercal} \begin{pmatrix} H_0 - \mu & \mathbf{\Delta} \\ \mathbf{\Delta}^{\dagger} & \mu - \mathcal{T} H_0 \mathcal{T}^{-1} \end{pmatrix} \mathbf{\Psi} \\ &\equiv \frac{1}{2} (\mathbf{\Psi}^{\dagger})^{\intercal} h_{BdG} \mathbf{\Psi}\end{aligned}$$

where the $2N \times 2N$ onsite Hamiltonian terms $H_e = H_0$ for an electron and H_h for a hole were introduced similarly as in the previous descriptions and where μ is the Fermi energy. The superconducting block is given by $\mathbf{\Delta} = \Delta \mathbb{1}_N \otimes \sigma_0$ where $\mathbb{1}_N$ is the $N \times N$ identity matrix. $\mathcal{T} = -i \mathbb{1}_N \otimes \sigma_y \mathcal{K}$ is the particle-hole symmetry operator, for which the derivation can be found in Appendix B. In a superconductor, the energy levels of holes are the symmetric of the energy levels of particles with respect to the Fermi energy. This characteristic is called particle-hole symmetry and can furthermore be seen directly in the hole Hamiltonian for which holds $H_h = -\mathcal{T} H_0 \mathcal{T}$.

In the numerical implementation of the model, Δ is assumed to be real. Also, the Bogoliubov-de Gennes Hamiltonian is provided for each site individually and applied to each lattice site. This results in the Hamiltonian for a site j:

$$\hat{H}_j = -\mu_{SC} (\hat{c}^{\dagger}_{j\uparrow} \hat{c}_{j\uparrow} + \hat{c}^{\dagger}_{j\downarrow} \hat{c}_{j\downarrow}) + \Delta (\hat{c}^{\dagger}_{j\uparrow} \hat{c}^{\dagger}_{j\downarrow} + \hat{c}_{j\downarrow} \hat{c}_{j\uparrow})$$

where the Fermi energy is taken at zero and μ_{SC} is the onsite potential. The Hamiltonian can be further simplified into:

$$h_{BdG} = \begin{pmatrix} -\mu_{SC} & \circ & \Delta & \circ \\ \circ & -\mu_{SC} & \circ & \Delta \\ \Delta & \circ & \mu_{SC} & \circ \\ \circ & \Delta & \circ & \mu_{SC} \end{pmatrix} = \begin{pmatrix} -\mu_{SC} \sigma_0 & \Delta \sigma_0 \\ \Delta \sigma_0 & \mu_{SC} \sigma_0 \end{pmatrix} = -\mu_{SC} \tau_z \otimes \sigma_0 + \Delta \tau_x \otimes \sigma_0$$

in the basis of $\mathbf{\Psi} = (\hat{c}_{\uparrow}, \hat{c}_{\downarrow}, \hat{c}^{\dagger}_{\downarrow}, -\hat{c}^{\dagger}_{\uparrow})^{\intercal}$. The hopping Hamiltonian in the superconductor is identical to the one described in the previous section, with a magnetic flux $\phi/\phi_0 = 0$ as no magnetic field enters the superconductor.

Chapter 3

Valley polarisation dependence of the NS conductance

In this chapter, the tight-binding systems described in the previous chapter are implemented numerically. For the normal (or metallic), magnetic and superconducting regimes, characteristic results will be derived to understand their individual effects. Finally, the existence of conductance plateaus for three normal-superconducting (NS) junction configurations is investigated for each graphene nanoribbon (GNR) edge type.

3.1. Geometry of a graphene nanoribbon

The lattice vectors and atoms basis can be set up in several ways. Because the considered systems will be horizontal GNRs, one is looking to combine the lattice vectors in such a way that translational symmetry is defined horizontally. Several combinations are shown in Figure 3.1.1 for both zigzag and armchair GNRs.

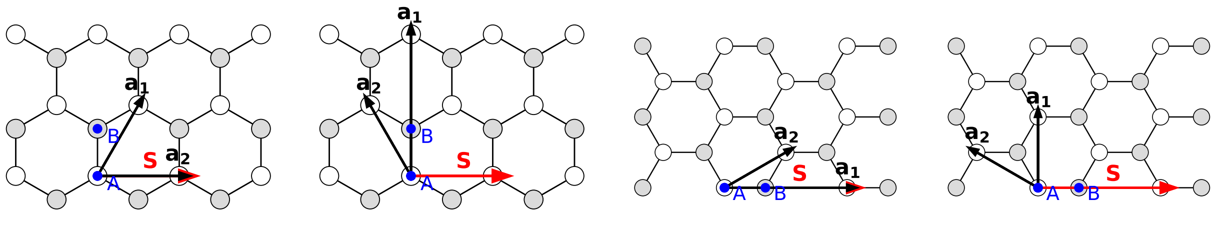

(a) $\mathbf{S} = \mathbf{a}_2$ (b) $\mathbf{S} = 2\mathbf{a}_1 - \mathbf{a}_2$ (c) $\mathbf{S} = \mathbf{a}_1$ (d) $\mathbf{S} = \mathbf{a}_1 - 2\mathbf{a}_2$

Figure 3.1.1: Graphene lattice with different primitive lattice vectors $\mathbf{a}_1$ and $\mathbf{a}_2$ and basis points A and B along with the symmetry vector $\mathbf{S}$, used as a parameter for the translational symmetry of the lattice.

Figure 3.1.2 shows that for the unit-cells from Figure 3.1.1a and c, skew ribbons are obtained. While this does not matter for the produced results, the geometries from Figure 3.1.1b and d will be maintained in the rest of the study for the sake of representation.

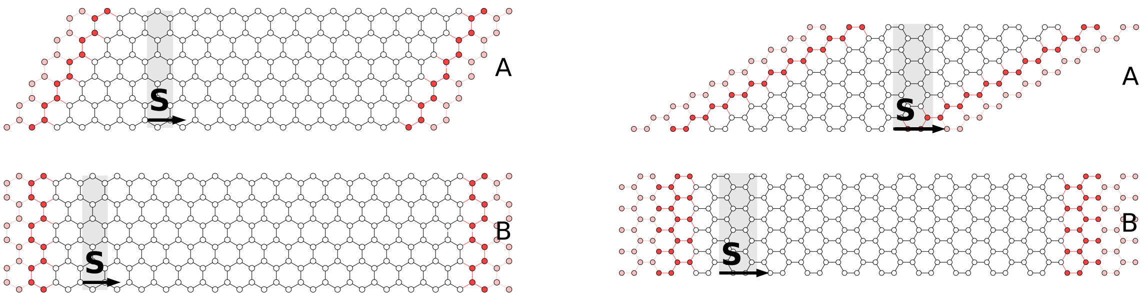

(a) Zig-zag edges

(b) Armchair edges

Figure 3.1.2: Example of a GNR W=8a generated with the respective geometries described in Figure 3.1.1. Zig-zag and armchair A are skew sheets and zig-zag and armchair B are rectangular. The grey area is the lattice period in the **S** direction.

3.2. Energy dispersion in graphene nanoribbons

The energy dispersion of normal graphene finite systems can be computed numerically by diagonalisation of the Hamiltonian. This computation is performed by Kwant[15]. Figure 3.2.1 shows the dispersion relation of a 30a wide GNR, for the zigzag and armchair edges respectively, along with the analytical expression for infinite systems from (2.1.12) at different projection angles. As the ribbon width goes to infinity, the dispersion relation converges to (2.1.12). However, for the zigzag edges, two highly degenerate flat bands appear at at the Fermi level independently of the ribbon width. This peculiar feature is characteristic of the zigzag edges. It follows that the zigzag edge ribbon is metallic.

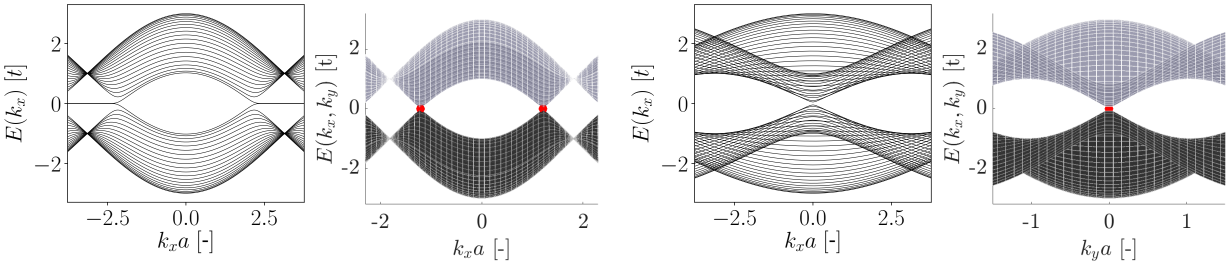

(a) Zigzag edge GNR.

(b) Armchair edge GNR.

Figure 3.2.1: In each subfigure, the numerically computed band structure for a 30a wide graphene nanoribbon (GNR) (left) and the surface plot of the tight-binding dispersion relation seen from a certain angle (right).

For armchair ribbons, in contrast, the ribbon is a conductor for some widths, and a semi-conductor for other widths. This behaviour is illustrated with an example in Figure 3.2.2.

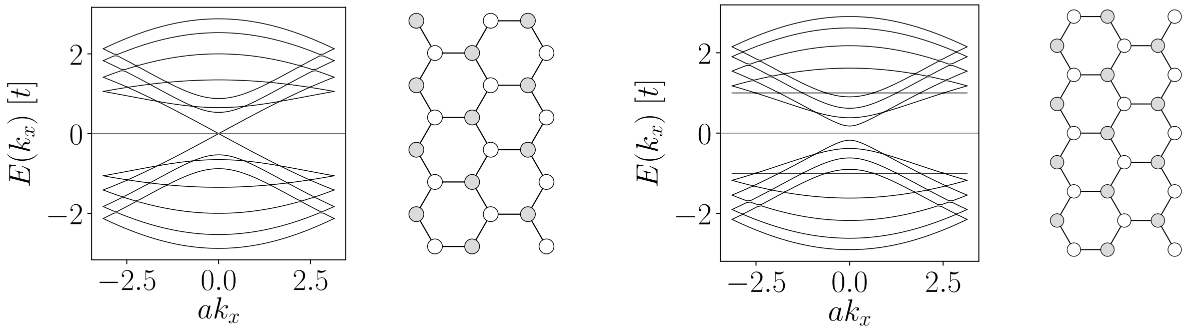

(a) Ribbon widths of four unit armchairs. This configuration is a conductor.

(b) Ribbon widths of five unit armchairs. This configuration is a semi-conductor.

Figure 3.2.2: Energy dispersion of an armchair-edge nanoribbon for two subsequent ribbon widths.

In fact, the ribbon width must follow a certain pattern in order to be metallic or semi-conductor. The conclusion was made from analytical results based on the Dirac equation and in the tight-binding approximation in [3, 46] that the ribbon becomes a conductor for widths which can be written as $3m + 1$ for $m \in \{0, 1, ...\}$, in units of armchair structures. The tight-binding result could be verified and compared with the analytic approximation, demonstrated in Figure 3.2.3 in accordance with the results found in [3]. This alternating pattern is due to the boundary conditions of armchair edges, which are different for three subsequent GNR widths as specified previously.

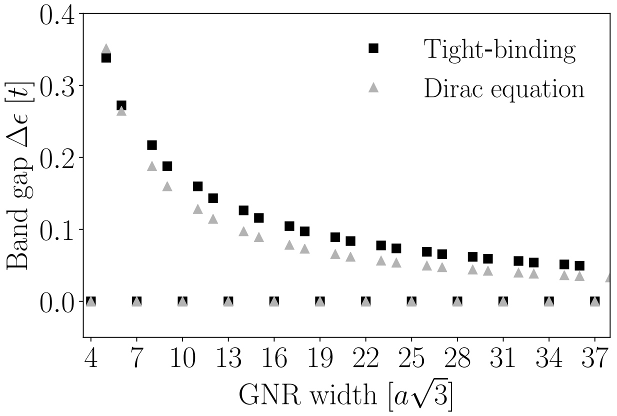

Figure 3.2.3: Band gap in a graphene ribbon with armchair edges as a function of the ribbon width. The band-gap becomes zero, i.e. the ribbon becomes metallic, at the $3m + 1$ widths.

3.3. Graphene nanoribbon under a magnetic field

As introduced in the Introduction of this thesis, we compute the dispersion relations of armchair and zigzag GNRs for different strengths of the magnetic field. A $101a$ wide armchair GNR, for which a nonzero bandgap occurs at no magnetic field, was taken in Figure 3.3.1 (top). For a nonzero magnetic field, the bandgap immediately becomes zero. The flat bands become increasingly wide with the magnetic field and the spacing between the bands increases with $\propto \sqrt{B}$. For extremely strong magnetic fields, the lowest band starts showing abnormalities. The zigzag edge GNR has the same properties, apart from the fact that at zero magnetic field a flat band is always present at the zero of energy. The obtained results are in agreement with results from literature[47, 11] and confirm the anomalous QHE of graphene (only half or less of the Brillouin zone is shown but it is symmetric in k-space).

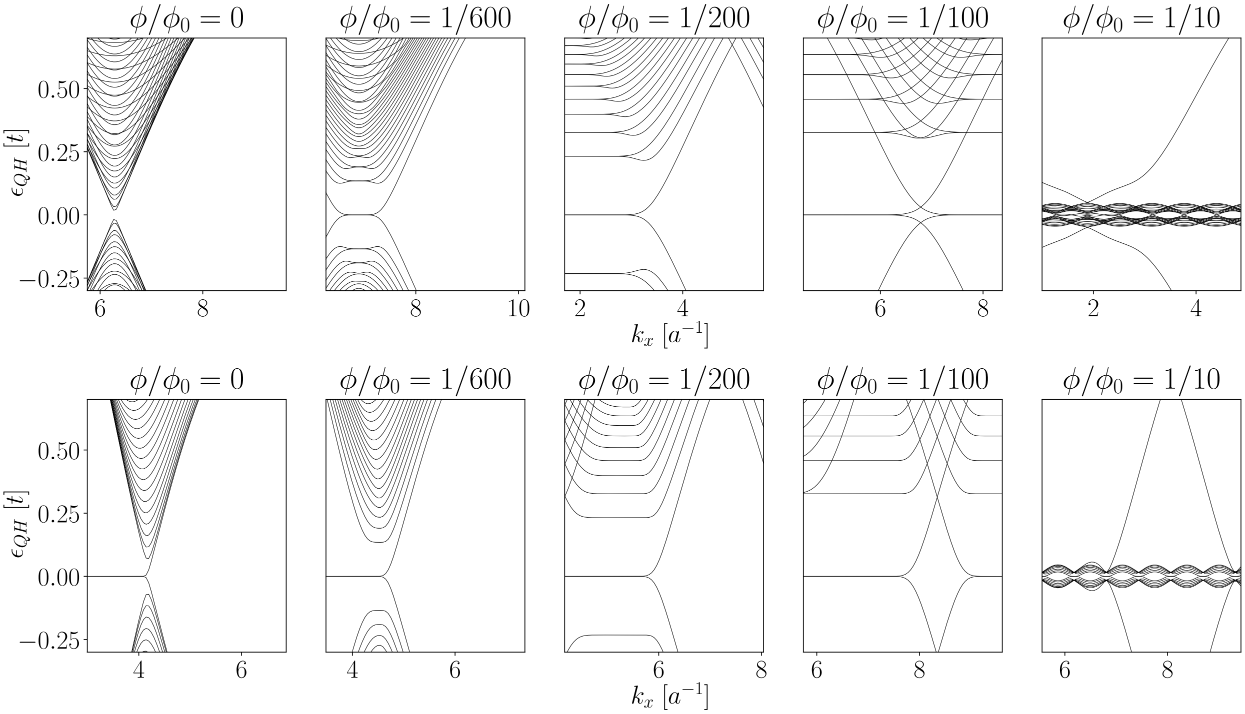

Figure 3.3.1: Band structure of an armchair (top) and zigzag (bottom) edge graphene nanoribbon for different values of the flux per plaquette ϕ/ϕ_0. The spacing between the Landau levels increases as predicted and the bands become increasingly wide.

3.4. Conductance of an NS junction

We propose a method to verify the theoretical prediction made in [5], for the conductance of a normal-superconducting (NS) junction in the lowest Landau level (LLL). The conductance G_{NS}, measured between the superconductor (SC) and the normal metal, is predicted to be:

$$G_{NS} = \frac{2e^2}{h}(1 - \cos\Theta) \tag{3.4.1}$$

where Θ is the relative angle between the valley isospins of the incoming and outgoing edge states. The spin degree of freedom is also omitted in the onsite Hamiltonian, so the $\otimes\sigma_0$ term is removed. The conductance (3.4.1) is corrected with a factor 1/2 since the band structure accounts for twice less conduction channels which results in $G_{NS} = (1 - \cos\Theta)e^2/h$ in the LLL.

Specifically, three systems are considered, each one consisting of a semi-infinite graphene nanoribbon (GNR) made of a normal lead and a scattering region in the Hall regime as demonstrated in Figure 3.4.1. A sheet of superconducting graphene is brought in contact with the scattering region, covering two opposed edges (Figure 3.4.1a), two adjacent edges (Figure 3.4.1b) or a single edge (Figure 3.4.1b). The latter configurations are investigated both for zigzag and armchair GNR. The values predicted in[5] are given in Table 3.1.

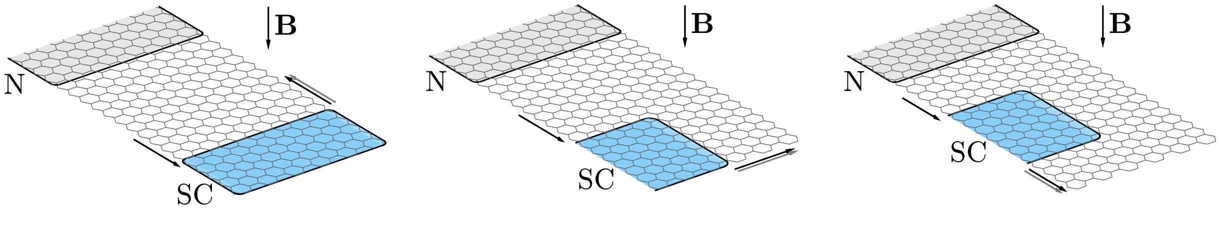

(a) Opposite edges (b) Adjacent edges (c) Single edge

Figure 3.4.1: NS junction made of a semi-infinite normal lead, a magnetic scattering region and a superconducting contact, for three positions of the superconductor. The horizontal arrows represent the edge states entering/leaving the superconductor. Hole states are represented with grey arrows and can leave the superconductor due to Andreev reflection.

Covering →	(a) opposed edges	(b) adjacent edges	(c) a single edge
Zigzag GNR	2	1	0
Armchair GNR	2 or 1/2	1	0

Table 3.1: Two-terminal conductance G_{NS} of a graphene NS junction in units of e^2/h for different positions of a superconducting sheet according to [5]. The bottom left cell is 2 (1/2) if the number of hexagons of an armchair GNR is (not) a multiple of three.

3.4.1. General model considerations

Several conditions must be verified by the NS junction[5] for equation (3.4.1) to be valid; the width of the system should be considerably larger than the magnetic length $Y \gg l_B = \sqrt{\hbar/eB}$ as a bulk region should allow for edge states to exist. The magnetic length should however be larger than the lattice constant $l_B \gg a$, in particular for the tight-binding approximation to be valid, and also to avoid anomalous Landau levels where number of bands around the Fermi energy becomes greater than two (cf. Figure 3.3.1). The chemical potential should be smooth along the direction of the dispersion, at the order of the lattice constant, in order to avoid additional scattering at a potential barrier. Also, the superconducting coherence length $\xi_0 = \hbar v_F/\Delta_0$ should be small compared to l_B for the effects of the magnetic field to be neglected in the superconducting region. The influence of these parameters on the conductance is investigated in the next chapter. In the current section, the validity of the theoretical predictions is verified using a tight-binding model of the junction.

The metallic normal region is simulated with heavily doped graphene, so modelled by a region with a relatively high chemical potential $\mu_N > \mu_{QH}$. Specifically, $\mu_N = -0.4t$. When specified explicitely, the strength of the magnetic field and the the superconducting order parameter are smoothed at the superconducting interface. The superconducting gap is kept at $\Delta = 0.05t$ which yields a superconducting coherence length of the order of $3a$. For magnetic fluxes per plaquette between $\phi/\phi_0 = 1/600$ and $1/200$, the magnetic length ranges from $l_B = 23a$ to $40a$.

3.4.2. Superconductor covering opposite edges

The magnetic field localises the wave function near the edges of the system to within a magnetic length while electrons with energies below the superconducting gap are Andreev reflected along the interface. The wave function for the opposite edges configuration is shown in Figure 3.4.2. The metallic lead was removed from the figure so only the quantum Hall region and the superconductor are represented.

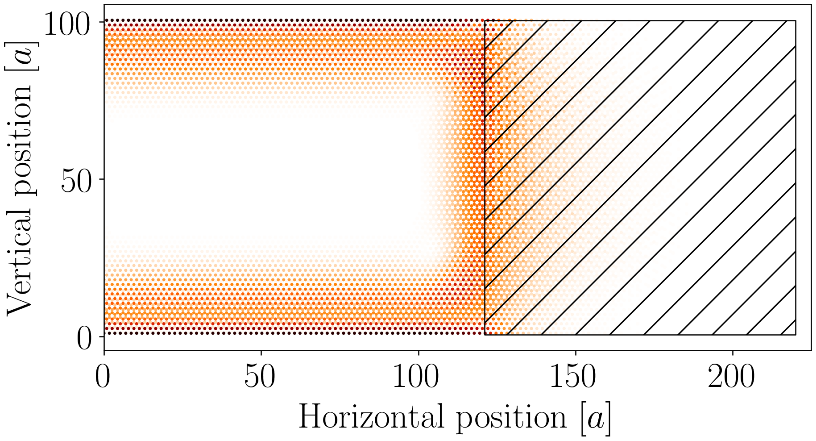

Figure 3.4.2: Squared amplitudes of the electron wave function in a zigzag GNR NS junction with a superconducting contact covering opposite edges (hatched region).

The computation of the conductance is performed using the transmission matrix provided by the Python library for quantum transport Kwant[15]. In the rest of the results it should be noted that it is evaluated at the zero of energy of the system. The resulting conductance is represented in Figure 3.4.3a for a zigzag GNR and in Figure 3.4.3b for both cases of the armchair GNR. The corresponding band structure of pure magnetic graphene is plotted in the same figures, showing that the plateau clearly lies in the LLL.

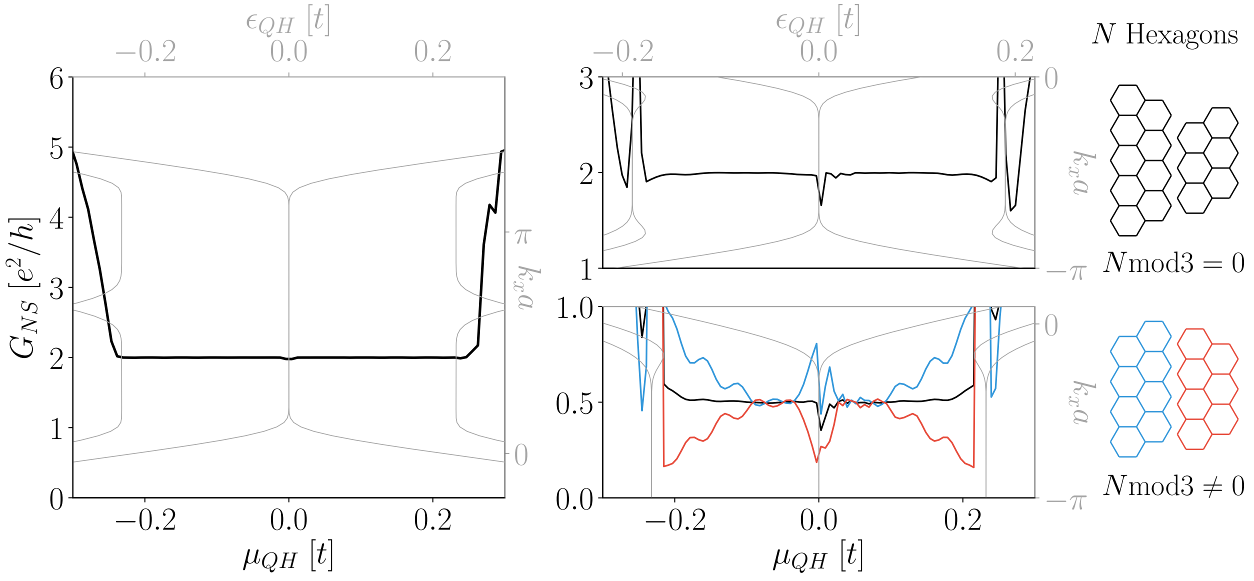

(a) Zigzag

(b) Armchair

Figure 3.4.3: Conductance plateaus of the NS junction (black) observed in the LLL, in agreement with [5]. The band structure of magnetic graphene for $\phi/\phi_0 = 1/200$ is plotted on top (gray). For the armchair 1/2 configuration, two subsequent GNR widths are represented (red and blue) along with their average (black). The width of the GNR was fixed at $100a$.

The conductance plateaus in the zigzag configuration were easily obtainable for a wide range of magnetic fields and relatively small systems. For armchair edges, in particular in the 1/2 case, a flat plateau seems impossible to obtain. In fact, the 1/2 armchair case presents a peculiar feature demonstrated in Figure 3.4.3b. The conductance of two subsequent armchair GNR widths, which are not a multiple of three hexagons high, is opposite w.r.t. $e^2/2h$ for each chemical potential (cf. Figure 3.4.3b). When averaging both conductance curves, a flat plateau at $G_{NS} = e^2/2h$ is obtained. Near the Fermi energy, irregularities are observed. In fact, the Hamiltonian in $\mu_{QH} = 0$ is singular so the conductance is never evaluated in this exact point.

3.4.3. Superconductor covering adjacent edges

If the superconductor covers adjacent edges of the GNR, conductance plateaus were confirmed to appear at $G_{NS} = 1e^2/h$ in the LLL both for armchair and zigzag edges as demonstrated in Figure 3.4.4. The superconducting gap and the magnetic field were smoothed over an interval $40a$ at the superconducting interface, as it was a necessary condition for obtaining plateaus. Too strong magnetic fields were observed to destabilise the plateau as well. The conditions imposed on these parameters will be further detailed in the next chapter. In general, the obtained plateaus for this case are not perfectly flat. Also, the conductance plateau for the zigzag edge GNR case was consistently observed to be between $1.1e^2/h$ and $1.21e^2/h$. Intervalley scattering is the expected cause for this higher conductance so armchair edge states are not perfectly valley polarised.

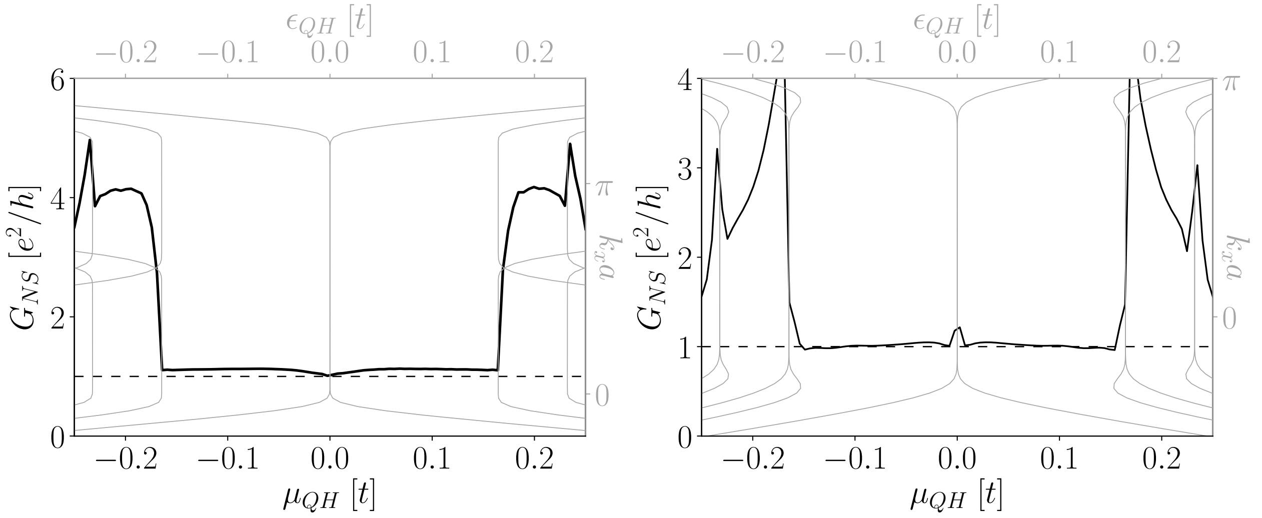

(a) Zigzag

(b) Armchair

Figure 3.4.4: Conductance of an NS junction in which the superconductor covers adjacent edges. The band structure of magnetic graphene for $\phi/\phi_0 = 1/400$ is plotted on top (gray). A dashed line indicates the expected conductance plateau in the lowest Landau level. The width of the GNR was fixed at $240a$.

3.4.4. Superconductor covering a single edge

When the superconductor covers a single edge of the GNR, a perfect plateau at $G_{NS} = 0$ was observed for zigzag edges, with a maximal deviation of $10^{-4}e^2/h$ from the predicted value. A flat plateau for armchair edges was observed with a maximal deviation of $10^{-2}e^2/h$.

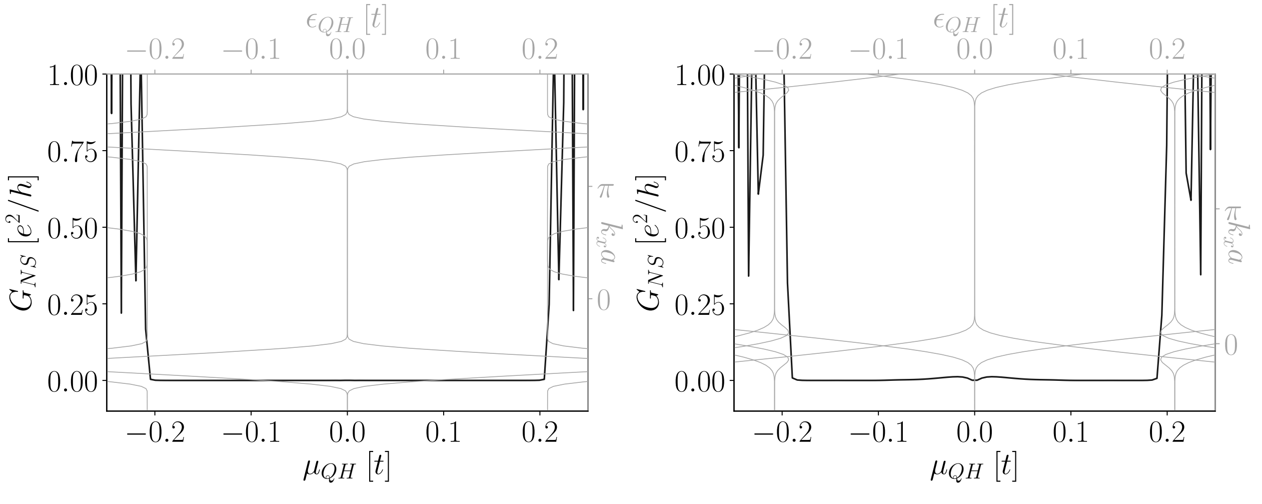

(a) Zigzag

(b) Armchair

Figure 3.4.5: Conductance of an NS junction in which the superconductor covers a single edge. The band structure of magnetic graphene for $\phi/\phi_0 = 1/250$ is plotted on top (gray). A dashed line indicates the expected conductance plateau in the lowest Landau level. The width of the GNR was fixed at $240a$.

Chapter 4

Robustness and parameter regimes

In this chapter, we investigate the effects of changing parameters in the junction on the conductance plateaus. The robustness of the edge modes is finally tested by adding potential at the NS interface. This allows to verify if the reason for deviations is intervalley scattering.

4.1. Parameter regimes

4.1.1. Size of the superconductor

The edge states entering the superconductor are described by the Bogoliubov-de Gennes equation in the model. The superconductor should be large enough at the scale of the characteristic lengths for the electron wave function to become zero in the superconductor. We consider the opposed edges case, with a zigzag edge GNR width W and a scattering region of length $140a + x_{SC}$, where x_{SC} is the length of the superconductor. The conductance for some point $\mu_{QH} = -0.1t$ in the LLL is computed for a range of superconductor lengths and shown in Figure 4.1.1. We find that for most GNR widths, $x_{SC} \geq 100a$ is a sufficient condition to obtain a conductance plateau.

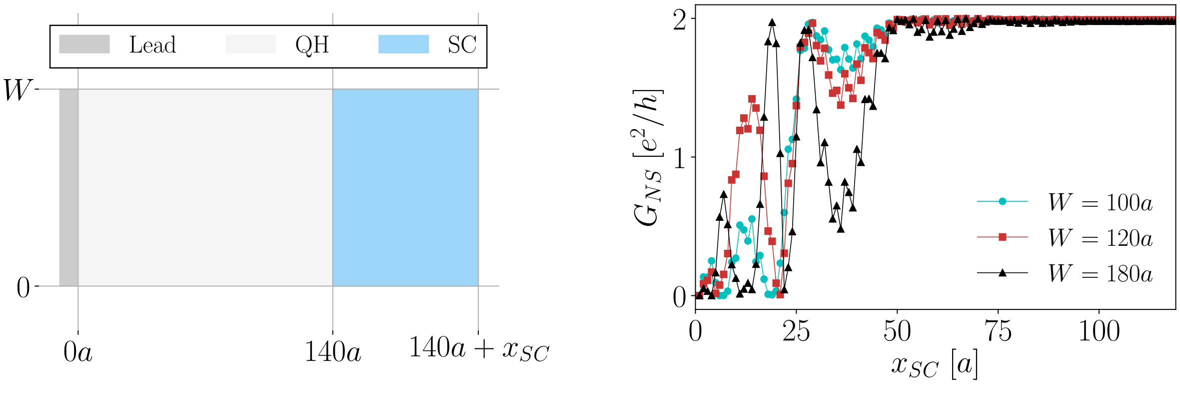

(a) Setup schematic

(b) Conductance at $\mu_{QH} = -0.1t$

Figure 4.1.1: Conductance of an NS junction with a superconductor covering opposite edges, evaluated at $\mu_{QH} = -0.1t$, for a range of lengths x_{SC} of the superconductor varied according to the schematic (left). This computation is conducted for three GNR widths (right).

4.1.2. Scale of the system

Considering an analogous configuration, we now vary the scale of the system. The ribbon width to scattering region length ratio is kept at 2.2 as demonstrated in Figure 4.1.2a. The conductance is then computed for different scales, each time for seven values of μ_{QH} in a small range of the LLL. The resulting conductance is provided in Figure 4.1.2b in a semi-logarithmic scale. The magnetic flux is kept at $\phi/\phi_0 = 1/200$ and no smoothing of parameters is used. A width of approximately $5l_B$ satisfies so these results confirm the requirement $W \gg l_B$ posed in [5].

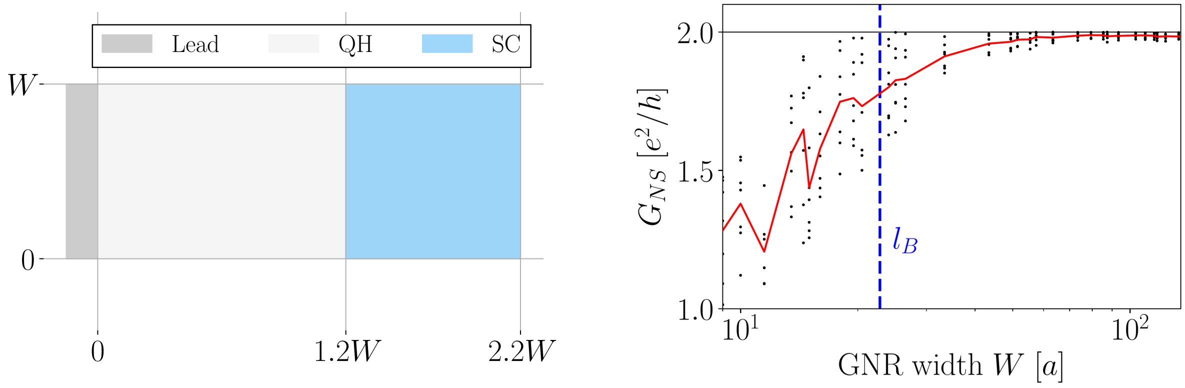

(a) Setup schematic

(b) Conductance at $\mu_{QH} \in [-0.15, -0.10]t$

Figure 4.1.2: For a range of scales, the conductance is evaluated at seven evenly spaced chemical potentials $\mu_{QH} \in [-0.15, -0.10]t \subseteq$LLL (black dots) in a zigzag graphene nanoribbon with a superconductor on opposed edges and a magnetic flux per plaquette $\phi/\phi_0 = 1/200$. The average of each set of seven points is also shown (red curve). The magnetic length is indicated with l_B (blue dashed line).

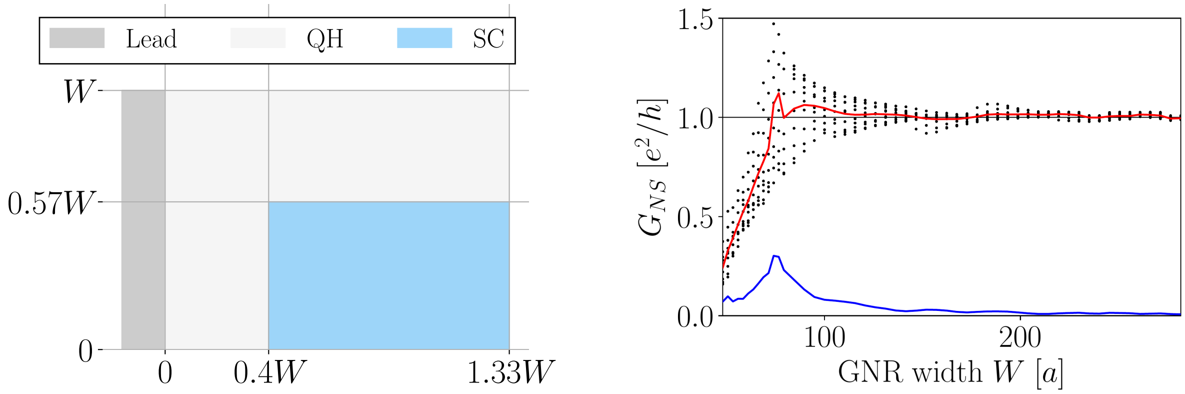

(a) Setup schematic

(b) Conductance at $\mu_{QH} \in [-0.13, -0.07]t$

Figure 4.1.3: For a range of scales, the conductance is evaluated at ten evenly spaced chemical potentials $\mu_{QH} \in [-0.13, -0.07]t \subseteq$LLL (black dots) in an armchair graphene nanoribbon with a superconductor (SC) covering adjacent edges. The average and standard deviation of each set of ten points is also shown (red and blue curves respectively). A smoothing interval of $_{\phi,\Delta} = 35a$ was used at the SC interface with $\phi/\phi_0 = 1/400$.

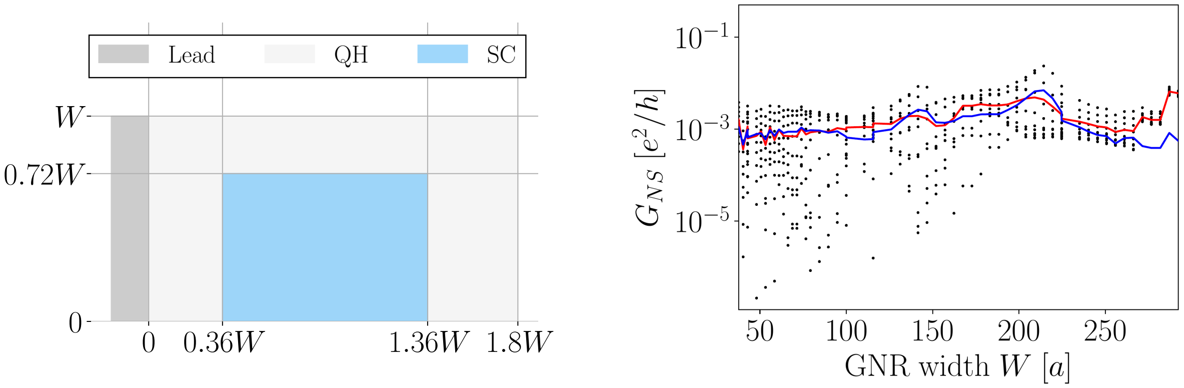

(a) Setup schematic

(b) Conductance at $\mu_{QH} \in [-0.13, -0.07]t$

Figure 4.1.4: For a range of scales, the conductance is evaluated at ten evenly spaced chemical potentials $\mu_{QH} \in [-0.13, -0.07]t \subseteq$LLL (black dots) in an armchair graphene nanoribbon with a superconductor (SC) covering a single edge. The average and standard deviation of each set of ten points is also shown (red and blue curves respectively). A smoothing interval of $_{\phi,\Delta} = 35a$ was used at the SC interface with $\phi/\phi_0 = 1/250$.

4.1.3. Smoothing intervals

Smoothing of parameters was found to have a negligible effect on the conductance in the opposite edges case. Smoothing of Δ and ϕ at the boundaries of the superconductor would nonetheless remove minor irregularities from a smoothing interval $\chi_{\phi,\Delta} \approx 10a$.

In the adjacent edges case, smoothing was found to be a crucial parameter for obtaining a conductance plateau. We first show that the wave function is unevenly distributed across the edges of the system for low smoothing intervals $\chi_{\phi,\Delta}$ of the magnetic field and the superconducting order parameter. This is demonstrated in Figure 4.1.5. This characteristic is particularly noticeable in the armchair case with $\chi_{\phi,\Delta} = 0$, where the probability of finding an electron is excessively strong at the upper boundary of the superconductor compared with the other boundaries. Figure 4.1.6 provides the conductance associated with each of these wave functions. A range of ten conductances was computed for a varying smoothing interval which confirms that there is a positive correlation between the formation of a plateau and the smoothing interval. Considering the convergence, it is confirmed that from a threshold smoothing interval approximately equal to $30a$, a plateau is formed. In the zigzag edge case, the standard deviation increases from $30a$ however, despite the fact that the mean continues to converge to e^2/h. This shows that there is a constant slope on the plateau, identical to the one observed in the $\chi_{\phi,\Delta} = 43a$ zigzag edge case.

The case with opposite edges shows comparable results shown in Figure 4.1.7. The convergence of the plateau to is much stronger than the adjacent edges case. The armchair edge case shows a converge to 1e−3 which agrees with the fact that intervalley scattering occurs in the armchair edge case.

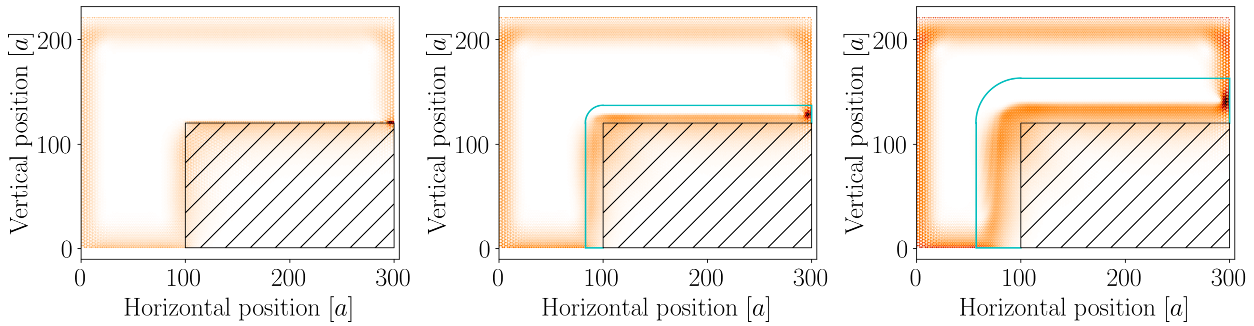

(a) Zigzag, $\chi_{\phi,\Delta} = 0$ (b) Zigzag, $\chi_{\phi,\Delta} = 17a$ (c) Zigzag, $\chi_{\phi,\Delta} = 43a$

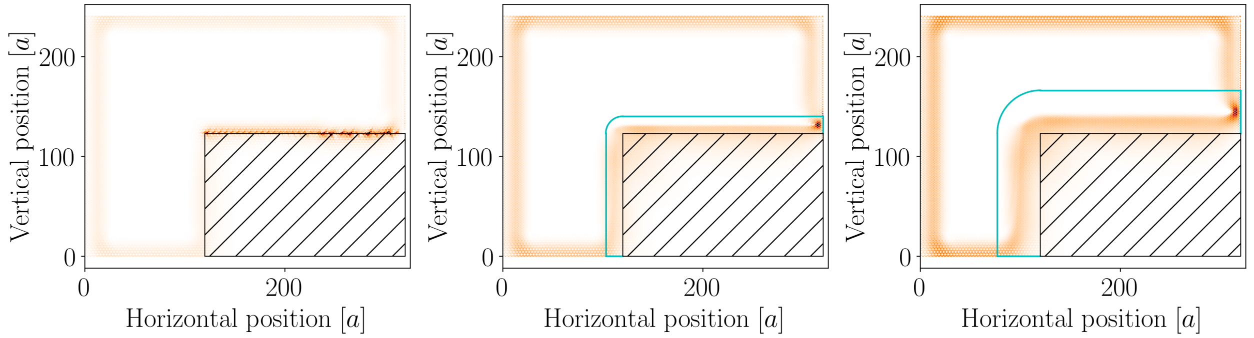

(d) Armchair, $\chi_{\phi,\Delta} = 0$ (e) Armchair, $\chi_{\phi,\Delta} = 17a$ (f) Armchair, $\chi_{\phi,\Delta} = 43a$

Figure 4.1.5: Amplitudes of the electron/hole wave function in a zigzag GNR NS junction with a superconducting contact (SC) covering adjacent edges (hatched region), for different smoothing intervals $\chi_{\phi,\Delta}$ (cyan curve) of the magnetic flux and the superconducting pairing potential. All cases are for $\phi/\phi_0 = 1/350$.

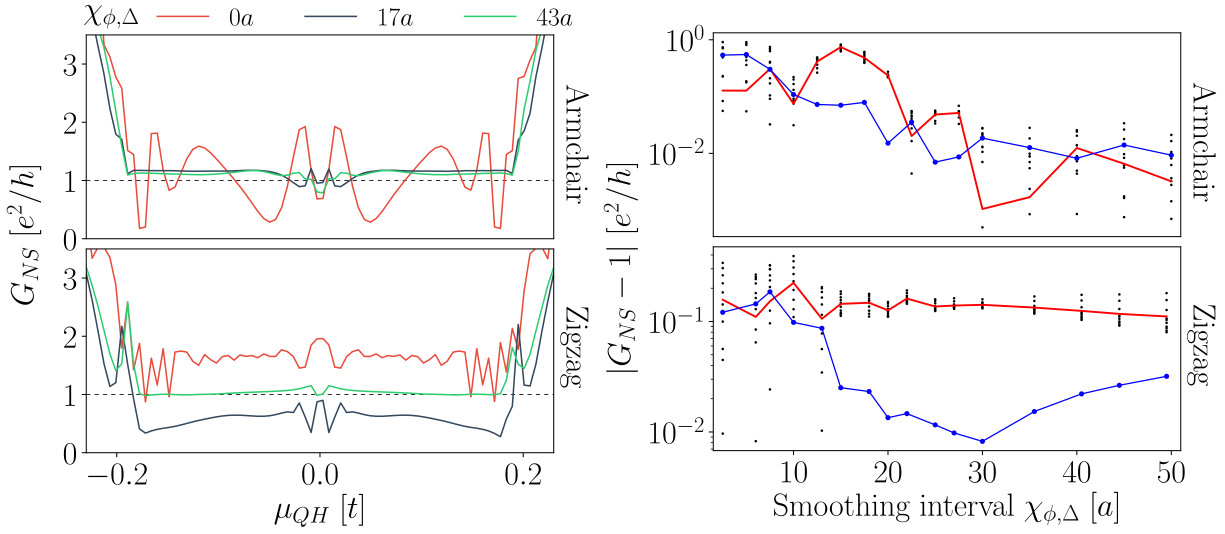

(a) Conductance in the LLL (b) Conductance at $\mu_{QH} \in [-0.15, -0.07]t$

Figure 4.1.6: (Left) Conductance of an NS junction in which the superconducting contact covers adjacent edges, for three different smoothing intervals. A flux per plaquette $\phi/\phi_0 = 1/300$ was used. (Right) Average (red), standard deviation (blue) and computed values (black) of the conductance for the same case, for ten evenly spaced values of μ_{QH}.

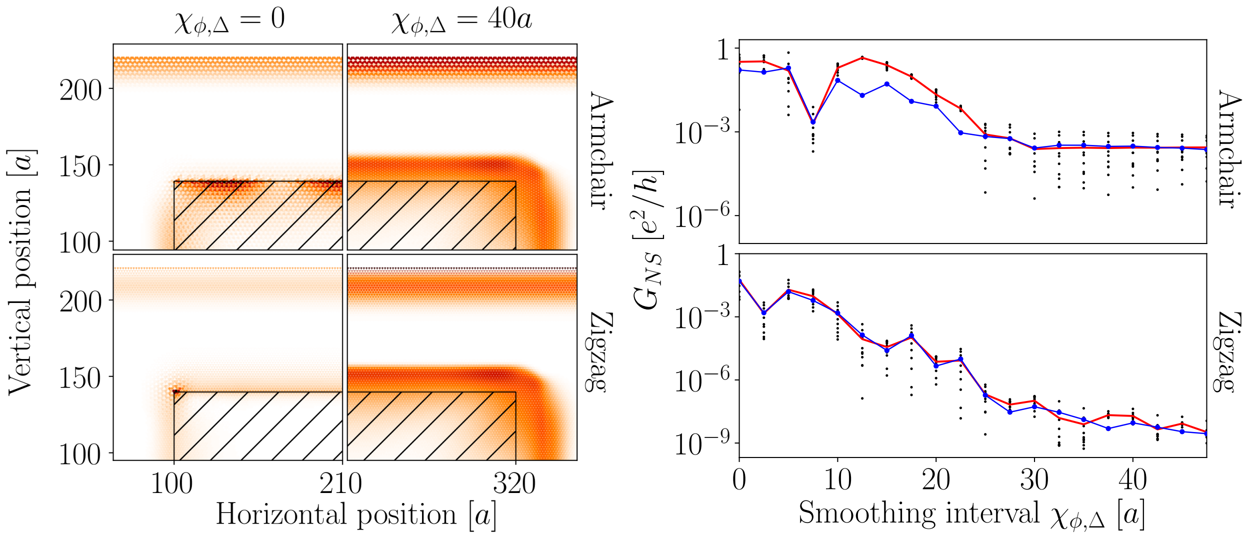

(a) Wave function

(b) Conductance at $\mu_{QH} \in [-0.13, -0.07]t$

Figure 4.1.7: (Left) Wave function for the case where the superconductor covers a single edge, for zero and nonzero smoothing interval of the magnetic flux and the superconducting pairing potential. Smoothing causes the wave function to be spread more evenly. (Right) Average (red), standard deviation (blue) and computed values (black) of the conductance for the same case, for ten evenly spaced values of μ_{QH} in $[-0.13, -0.07]t$.

4.2. Disordered NS interface

In the previous section, we have shown that smoothing of the magnetic field and the superconducting order parameter allows for the occurrence of plateaus. Also, the Fermi energy in the scattering region was kept uniform by assuming $\mu_{QH} = \mu_{SC}$. In this section, disorder is added at the NS interface to test the robustness of the edge states. In the first part, the chemical potential in the superconductor is fixed. In the second part, uncorrelated disorder potential is added and quantified with the standard deviation of a normal distribution. In the second part, disorder is modelled with an electrostatic potential landscape quantified by a correlator between the sites of the lattice.

4.2.1. Fermi energy mismatch at the NS interface

The predictions from Akhmerov & Beenakker[5] are expected to break down when the chemical potential changes discontinuously: in reciprocal space, the incoming states are scattered into many different momenta. To test whether the NS edge states are valley polarised, we look at the effect of smoothing the potential step, with $\mu_{SC} = 0.3t$ fixed. Because the smoothing of magnetic field and superconducting gap are required by the prediction, the smoothing of the chemical potential is done simultaneously. If done differently, different smoothing intervals of different quantities are mixed at the boundaries which could bias the results in an undesired way. Figure 4.2.1a shows that smoothing ϕ, Δ, μ_{SC} at the interface recovers the plateaus for a zigzag edge GNR. Intervalley scattering is stronger in the adjacent edges case and weak in the opposite edges and single edge case. For the armchair edges case Figure 4.2.1b, the $3N$ hexagons opposite edges case is particularly stable: a plateau is already recovered for very small smoothing intervals. The NS interface for this case is exclusively a zigzag edge, which lies in a single valley. This state is therefore less prone to intervalley scattering. More interestingly, the $3N+1$ and $3N+2$ hexagons cases are, as discussed before, perfectly "anti" valley polarised. The results are hardly plateaus for both cases but their average is a plateau even for smoothing intervals as small as $3a$. The adjacent edges and single edge cases show a slower convergence to the predicted result showing that the edge states are less robust in these cases as expected.

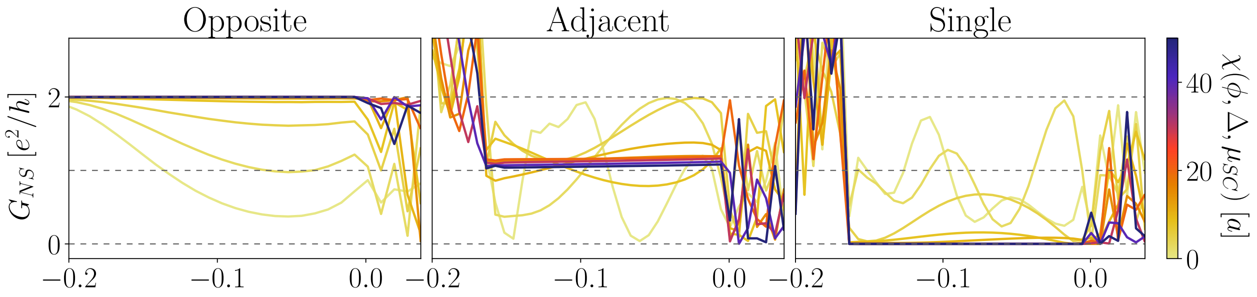

(a) Zigzag edge case.

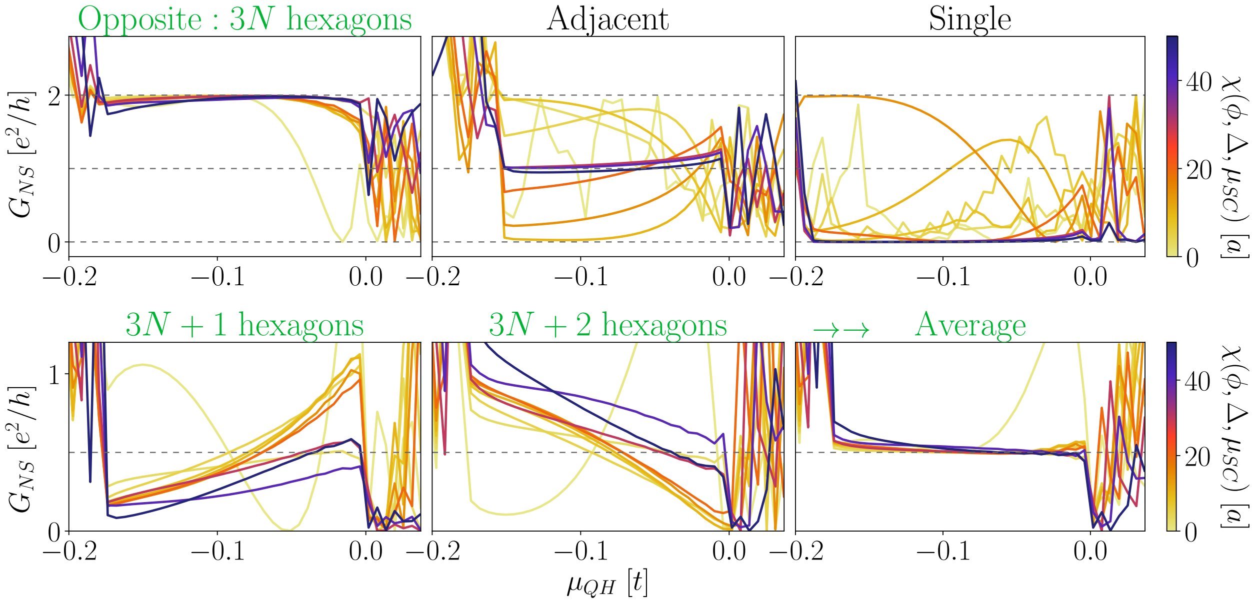

(b) Armchair edge case, where three cases for the opposite edges case are shown (green titles) with a fourth case corresponding to the average of the $3N+1$ and $3N+2$ opposite edges case.

Figure 4.2.1: Effect of smoothing the magnetic field, the superconducting gap and the chemical potential at the NS interface on the intervalley scattering of the NS edge modes, for the zigzag edges case (top) and armchair case (bottom), each for three cases: a superconductor covering opposite, adjacent or a single edge(s) of the nanoribbon.

The fact that three parameters are smoothed at the same time makes the interpretation of the conclusions about the NS edge modes uncertain. In the next section, another method is therefore proposed to qualify the intervalley scattering where only the potential is involved.

4.2.2. Uncorrelated disorder potential

We investigate the effect of adding normally distributed fluctuations in the onsite potential on the conductance plateaus obtained in the previous chapter. This potential is not correlated between different sites. The control parameters for these random fluctuations are therefore the mean of the normal distribution - fixed at zero, the standard deviation σ - varied between 0 and $0.1t$, and the region in which disorder is added - which is fixed at an interval of $40a$ between the quantum Hall region and the superconductor. The onsite reduced Hamiltonian used in this case is therefore:

$$h_j = -(\mu_j + \mu_{imp}) \cdot \tau_z + \Delta \cdot \tau_x \tag{4.2.1}$$

with $\mu_{imp} \sim N(\mu = 0, \sigma^2)$ and where the basis is the same as introduced in Chapter 2. The smoothing interval of the magnetic field and superconducting order parameter is taken at $40a$ as well, so that the NS interface is completely within the disordered region.

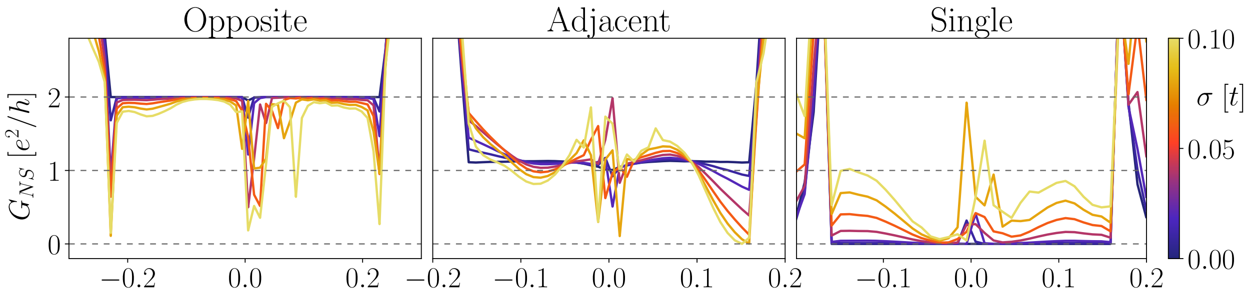

(a) Zigzag edge case.

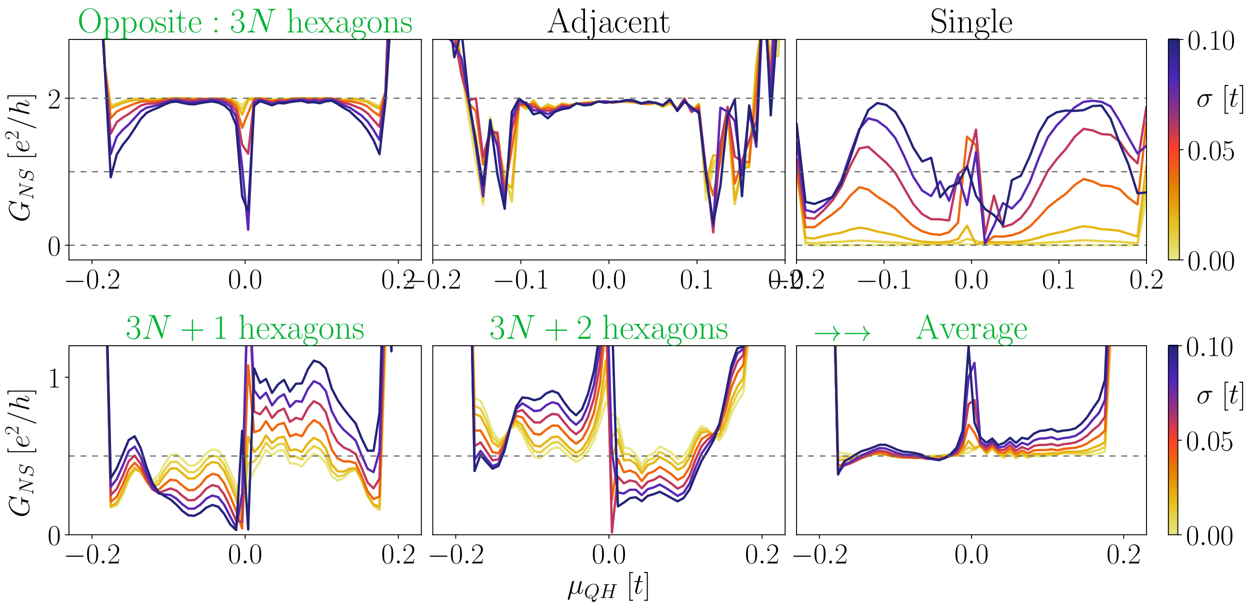

(b) Armchair edge case, where three cases for the opposite edges case are shown (green titles) with a fourth case corresponding to the average of the $3N+1$ and $3N+2$ opposite edges case.

Figure 4.2.2: Effect of increasing the standard deviation of a normally distributed random potential fluctuation on each lattice site, for a zigzag (top) and armchair (bottom) edge junction.

The location of each site is used a seed in the random variable generator so that only the effect of local deviations in the electrostatic potential is appreciated. Similar conclusions can be drawn from the previous results.

One distinguishing feature of the $3N+1$ and $3N+2$ cases of the armchair edge GNR is the fact that in both cases, the particle hole symmetry is broken (we could almost think about it as particle hole "anti-symmetry" here). When the $3N+1$ case is below the predicted value, the $3N+2$ is above the predicted value by the same amount. When looking at this behaviour in the BTK picture, one could think that in the $3N+1$ case, the probability of a hole being reflected back is exactly equal to the probability of an electron being reflected back in the $3N+2$ case. At first sight, this behaviour seems to correspond to the classical representation of Andreev reflection: the skipping orbits alternate between electron and hole so when a hole is reflected back in the $3N+1$ case, an electron must be reflected back in the $3N+2$ case. This interpretation is flawed since the classical picture does not explain the fact that the alternation is between A and B sites of the NS interface. However, recalling that Andreev reflection in graphene converts an electron from one valley into a hole from the other valley[6], and that each sublattice atom A and B is coupled to one of the valleys, adding an atom A or B at the interface will determine whether or not the reflected charge carrier is an electron.

4.2.3. Disorder potential landscape

Going a step further, we can look at the robustness of the edge modes in some smooth potential landscape. When modelling disorder with an electrostatic potential landscape, the control parameter is no longer the standard deviation of the random variables but a correlator which we introduce here based on a method provided in [7, 48]. The fluctuation in the chemical potential at a site j is taken as its convolution with a Gaussian potential:

$$\mu_{imp}(\mathbf{R}_j) = \sum_{i=1}^{N} \mu_i \exp\left(-\frac{|\mathbf{R}_j - \mathbf{R}_i|^2}{2\xi^2}\right) \tag{4.2.2}$$

where N is the number of sites in the disordered region, ξ is the length scale over which the Gaussian is smooth and $\mu_i \sim U(-\sigma, \sigma)$ is uniformly distributed.

$$K_0 = \frac{1}{N}\frac{LW}{(\hbar v_F)^2}\sum_{i=1}^{N}\sum_{j=1}^{N}\langle \mu_{imp}(\mathbf{R_i})\mu_{imp}(\mathbf{R_j})\rangle \tag{4.2.3}$$

In Figure 4.2.3 the wave function at the NS interface is computed for different values of σ and of ξ, showing how the edge states change in a random landscape. The produced edge states for most of the cases are destroyed so when looking at the conductance, we look at much weaker disorder.

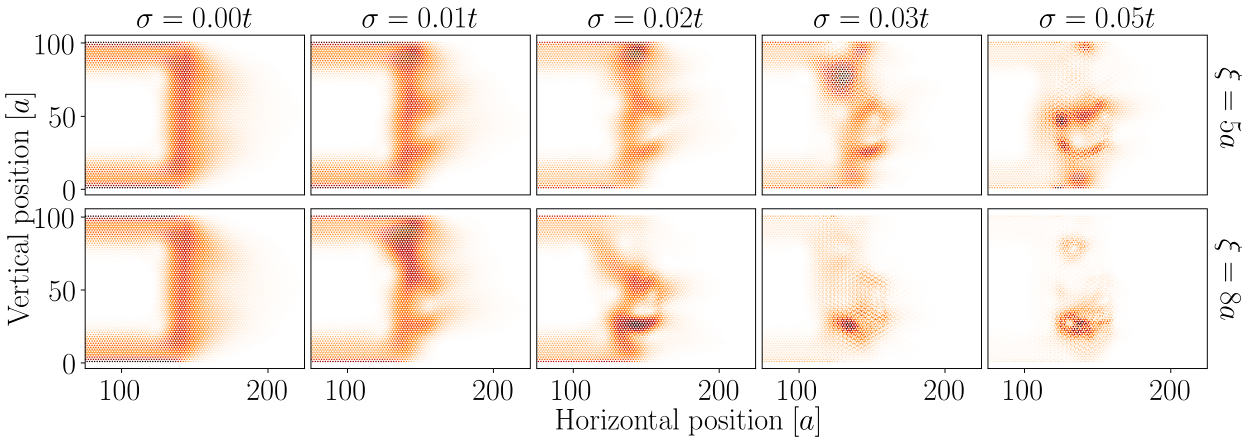

Figure 4.2.3: Wave function at the NS interface for different interval widths σ of the uniform distribution generating random potential deviations, and of ξ, the standard deviation of the Gaussian convoluted with the lattice sites.

Chapter 5

Conclusions

In this study, the realisation of simulations on the conductance in a graphene tight-binding system were achieved. The tight-binding Hamiltonian of normal graphene was derived, using first quantisation and second quantisation formalism. By means of a Peierls substitution, the tight-binding Hamiltonian of graphene in the quantum Hall regime was given, including the particle-hole degree of freedom. Using the Bogoliubov-de Gennes equation, the tight-binding model of a mean field S-wave superconductor was finally derived. Graphene nanoribbons with different edges were then implemented for each regime from which results already obtained in literature could be confirmed. The three tight-binding systems were finally combined to simulate the conductance in an NS junction, in which the superconductor was placed in three different configurations, for the two different junction edges, resulting in six different configurations. The conductance plateaus predicted in Akhmerov & Beenakker (2006)[5] could be confirmed for most configurations and the parameter ranges were tested subsequently, confirming that the results hold under the assumption of a smooth interface and a large system. It was shown that edge states in the adjacent edges case are not perfectly valley polarised. Disorder was added at the interface with a Fermi energy mismatch, random onsite potential fluctuations and with a random potential landscape, all confirming that NS edge states are valley polarised.

The armchair edge case was observed to deviate from the theory in a peculiar way. A plateau at $2e^2/h$ was obtained when the GNR was a multiple of three hexagons wide, in accordance with the theory[5], but poor plateaus were obtained for other widths. Instead, the conductance of two subsequent widths $3N+1$ and $3N+2$ were found to be symmetric with respect to $e^2/2h$. The reason for the deviation from the plateau is expected to be intervalley scattering, and the cause for the symmetry was hypothesised to be because of the nature of the Andreev reflected charge carrier; when a hole is reflected back in the $3N+1$ case, an electron must be reflected back in the $3N+2$ case which have perfectly opposite contributions to the BTK conductance. It was hypothesised that the cause for the complementary is that for a zigzag NS interface, each valley is coupled to a sublattice, while Andreev reflection in graphene converts electrons into holes from opposite valleys. By adding an atom from one sublattice to the edge, the electron tunneling to the newly added sublattice must be converted into a hole from the other valley because of the special Andreev reflection occuring in graphene.

- The reason for the symmetrical conductance in the opposed edges armchair case can be further investigated with theory

- The conductance obtained in the higher Landau levels can be investigated empirically using identical computations
- The effect of irregular edges at the NS interface can be investigated, as well as different angles with the superconductor

Bibliography

[1] A. Rycerz, J. Tworzydło, and C. Beenakker, "Valley filter and valley valve in graphene," *Nature Physics*, vol. 3, no. 3, p. 172, 2007.

[2] C. W. J. Beenakker, N. V. Gnezdilov, E. Dresselhaus, V. P. Ostroukh, Y. Herasymenko, i. d. I. Adagideli, and J. Tworzydło, "Valley switch in a graphene superlattice due to pseudo-andreev reflection," *Phys. Rev. B*, vol. 97, p. 241403, Jun 2018.

[3] L. Brey and H. A. Fertig, "Electronic states of graphene nanoribbons studied with the dirac equation," *Phys. Rev. B*, vol. 73, p. 235411, Jun 2006.

[4] C. Beenakker, "*Colloquium*: Andreev reflection and Klein tunneling in graphene," *Reviews of Modern Physics*, vol. 80, no. 4, p. 1337, 2008.

[5] A. R. Akhmerov and C. W. J. Beenakker, "Detection of valley polarization in graphene by a superconducting contact," *Phys. Rev. Lett.*, vol. 98, p. 157003, Apr 2007.

[6] C. W. J. Beenakker, "Specular andreev reflection in graphene," *Phys. Rev. Lett.*, vol. 97, p. 067007, Aug 2006.

[7] J. Tworzydło, I. Snyman, A. R. Akhmerov, and C. W. J. Beenakker, "Valley-isospin dependence of the quantum hall effect in a graphene $p-n$ junction," *Phys. Rev. B*, vol. 76, p. 035411, Jul 2007.

[8] C. Handschin, P. Makk, P. Rickhaus, R. Maurand, K. Watanabe, T. Taniguchi, K. Richter, M.-H. Liu, and C. Schonenberger, "Giant valley-isospin conductance oscillations in ballistic graphene," *Nano letters*, vol. 17, no. 9, pp. 5389–5393, 2017.

[9] L. Zhao, E. G. Arnault, A. Bondarev, A. Seredinski, T. Larson, A. W. Draelos, H. Li, K. Watanabe, T. Taniguchi, F. Amet, *et al.*, "Interference of chiral andreev edge states," *arXiv preprint arXiv:1907.01722*, 2019.

[10] D. R. Cooper, B. D'Anjou, N. Ghattamaneni, B. Harack, M. Hilke, A. Horth, N. Majlis, M. Massicotte, L. Vandsburger, E. Whiteway, *et al.*, "Experimental review of graphene," *ISRN Condensed Matter Physics*, vol. 2012, 2012.

[11] A. H. Castro Neto, F. Guinea, N. M. R. Peres, K. S. Novoselov, and A. K. Geim, "The electronic properties of graphene," *Rev. Mod. Phys.*, vol. 81, pp. 109–162, Jan 2009.

[12] S. H. Simon, *The Oxford solid state basics.* OUP Oxford, 2013.

[13] P. R. Wallace, “The band theory of graphite,” *Physical Review*, vol. 71, no. 9, p. 622, 1947.

[14] K. S. Novoselov, A. K. Geim, S. Morozov, D. Jiang, M. I. Katsnelson, I. Grigorieva, S. Dubonos, Firsov, and AA, “Two-dimensional gas of massless dirac fermions in graphene,” *Nature*, vol. 438, no. 7065, p. 197, 2005.

[15] C. W. Groth, M. Wimmer, A. R. Akhmerov, and X. Waintal, “Kwant: a software package for quantum transport,” *New Journal of Physics*, vol. 16, no. 6, p. 063065, 2014.

[16] J. D. Hunter, “Matplotlib: A 2d graphics environment,” *Computing in science & engineering*, vol. 9, no. 3, p. 90, 2007.

[17] MathWorks Inc., “MATLAB Version 9.5.0 (R2018b).” [Computer software], Natick, Massachusetts, 2018.

[18] J. R. Johansson, P. D. Nation, and F. Nori, “Qutip 2: A python framework for the dynamics of open quantum systems,” *Computer Physics Communications*, vol. 184, no. 4, pp. 1234–1240, 2013.

[19] E. Hall, “On a new action of the magnet on electric currents,” *American Journal of Science*, no. 111, pp. 200–205, 1880.

[20] K. von Klitzing, “The quantized hall effect,” *Rev. Mod. Phys.*, vol. 58, pp. 519–531, Jul 1986.

[21] P. Lederer and M. O. Goerbig, “Introduction to the quantum hall effects,” *Lecture Notes, Laboratoire de Physique des Solides, Université de Paris Sud*, 2006.

[22] Y. Zheng and T. Ando, “Hall conductivity of a two-dimensional graphite system,” *Phys. Rev. B*, vol. 65, p. 245420, Jun 2002.

[23] Z. Jiang, Y. Zhang, Y.-W. Tan, H. Stormer, and P. Kim, “Quantum hall effect in graphene,” *Solid state communications*, vol. 143, no. 1-2, pp. 14–19, 2007.

[24] D. Tong, “The Quantum Hall Effect. TIFR Infosys Lectures,” *Centre for Mathematical Sciences, Cambridge*, 2016.

[25] H. K. Onnes, “Further experiments with liquid helium,” in *KNAW, Proceedings*, vol. 13, pp. 1910–1911, 1911.

[26] J. Bardeen, L. N. Cooper, and J. R. Schrieffer, “Theory of superconductivity,” *Physical review*, vol. 108, no. 5, p. 1175, 1957.

[27] R. P. Feynman, R. Leighton, and M. Sands, “Lectures on Physics, volume III: Quantum mechanics, Chapter 21: The Schrödinger Equation in a Classical Context: A Seminar on Superconductivity,” *Reading, Ma.: Addison-Wesley*, 1965.

[28] M. Tinkham, *Introduction to superconductivity.* Courier Corporation, 2004.

[29] R. Holm and W. Meissner, "Messungen mit Hilfe von flüssigem Helium. XIII," *Zeitschrift für Physik*, vol. 74, no. 11-12, pp. 715–735, 1932.

[30] H. B. Heersche, P. Jarillo-Herrero, J. B. Oostinga, L. M. Vandersypen, and A. F. Morpurgo, "Induced superconductivity in graphene," *Solid State Communications*, vol. 143, no. 1-2, pp. 72–76, 2007.

[31] Y. Cao, V. Fatemi, S. Fang, K. Watanabe, T. Taniguchi, E. Kaxiras, and P. Jarillo-Herrero, "Unconventional superconductivity in magic-angle graphene superlattices," *Nature*, vol. 556, no. 7699, p. 43, 2018.

[32] A. Andreev, "The thermal conductivity of the intermediate state in superconductors," *Sov. Phys. JETP*, vol. 19, no. 15, pp. 1228–1231, 1964.

[33] I. O. Kulik and R. Ellialtiogammalu, *Quantum mesoscopic phenomena and mesoscopic devices in microelectronics*, vol. 559. Springer Science & Business Media, 2012.

[34] G. E. Blonder, M. Tinkham, and T. M. Klapwijk, "Transition from metallic to tunneling regimes in superconducting microconstrictions: Excess current, charge imbalance, and supercurrent conversion," *Phys. Rev. B*, vol. 25, pp. 4515–4532, Apr 1982.

[35] S. Reich, J. Maultzsch, C. Thomsen, and P. Ordejón, "Tight-binding description of graphene," *Phys. Rev. B*, vol. 66, p. 035412, Jul 2002.

[36] N. Ashcroft and N. Mermin, *Solid state physics*. Science: Physics, Saunders College, 1976.

[37] M. Born and R. Oppenheimer, "Zur quantentheorie der molekeln," *Annalen der physik*, vol. 389, no. 20, pp. 457–484, 1927.

[38] A. Altland and B. D. Simons, *Condensed matter field theory*. Cambridge University Press, 2010.

[39] Y. Oreg, "Concepts of condensed matter physics, Spring 2015 (Tutorial 1)," *Condensed Matter Physics, Weizmann Institute of Science*, 2015.

[40] I. Harald and H. Lüth, "Solid-state physics, an introduction to principles of materials science," 1996.

[41] W. Kohn, "Theory of bloch electrons in a magnetic field: The effective hamiltonian," *Phys. Rev.*, vol. 115, pp. 1460–1478, Sep 1959.

[42] K. Jimenez-Garcia, L. J. LeBlanc, R. A. Williams, M. C. Beeler, A. R. Perry, and I. B. Spielman, "Peierls substitution in an engineered lattice potential," *Physical review letters*, vol. 108, no. 22, p. 225303, 2012.

[43] E. Grosfeld, "Introduction to Localization," *Lecture notes in Solid State 3, Physics Department, Ben-Gurion University of the Negev*, 2016.

[44] H. V. Henderson and S. R. Searle, “The vec-permutation matrix, the vec operator and kronecker products: A review,” *Linear and multilinear algebra*, vol. 9, no. 4, pp. 271–288, 1981.

[45] J.-X. Zhu, *Bogoliubov-de Gennes method and its applications*, vol. 924. Springer, 2016.

[46] Y.-W. Son, M. L. Cohen, and S. G. Louie, “Energy gaps in graphene nanoribbons,” *Phys. Rev. Lett.*, vol. 97, p. 216803, Nov 2006.

[47] K. Wakabayashi, M. Fujita, H. Ajiki, and M. Sigrist, “Electronic and magnetic properties of nanographite ribbons,” *Physical Review B*, vol. 59, no. 12, p. 8271, 1999.

[48] A. Rycerz, J. Tworzydło, and C. W. J. Beenakker, “Anomalously large conductance fluctuations in weakly disordered graphene,” *Europhysics Letters (EPL)*, vol. 79, p. 57003, jul 2007.

[49] D. J. Griffiths, *Introduction to Quantum Mechanics (2nd Edition).* Pearson Prentice Hall, 2nd ed., 2004.

[50] S. Pathak, “An Introduction to Second Quantization,” *Course for Advanced Solid State Physics, Louisiana State University*, 2010.

[51] F. Utermohlen, “Tight-binding model in the second quantization formalism,” *Ohio State University*, 2018.

Appendix A

Formalism

A.1. Second quantisation

The underneath is a short summary of an extract of Chapter 2 in [38] and some other sources, which introduces second quantisation. More can be found in [38].

A.1.1. Motivation: Many-particle wave functions

If one considers a system of two distinguishable particles, one in state ψ_1 at position $\mathbf{r}_1$ and the other in ψ_2 at a location $\mathbf{r}_2$, the total wave function is given by:

$$\Psi(\mathbf{r}_1, \mathbf{r}_2) = \psi_1(\mathbf{r}_1)\psi_2(\mathbf{r}_2) \equiv |\lambda_1\rangle \otimes |\lambda_2\rangle$$

where spin is ignored for the moment. If the particles are indistinguishable, the two particle system must be in a superposition of the states which remains identical under the permutation operator. This condition is met by two wave functions:

$$\Psi(\mathbf{r}_1, \mathbf{r}_2) = \frac{1}{\sqrt{2}}\left(\psi_1(\mathbf{r}_1)\psi_2(\mathbf{r}_2) + \zeta\psi_2(\mathbf{r}_1)\psi_1(\mathbf{r}_2)\right) \equiv \frac{1}{\sqrt{2}}(|\lambda_1\rangle \otimes |\lambda_2\rangle + \zeta\,|\lambda_2\rangle \otimes |\lambda_1\rangle)$$

where $\zeta = -1$ for fermions and $\zeta = +1$ for bosons accounts as the symmetrization requirement[49]. Similarly, the wave function of a system of three indistinguishable particles is given by (omitting the ket notation):

$$\begin{aligned}\Psi(\mathbf{r}_1, \mathbf{r}_2, \mathbf{r}_3) = \frac{1}{\sqrt{3!}}(&\psi_1(\mathbf{r}_1)\psi_2(\mathbf{r}_2)\psi_3(\mathbf{r}_3) + \zeta\psi_1(\mathbf{r}_1)\psi_3(\mathbf{r}_2)\psi_2(\mathbf{r}_3) + \zeta\psi_2(\mathbf{r}_1)\psi_1(\mathbf{r}_2)\psi_3(\mathbf{r}_3) \\ &+\psi_2(\mathbf{r}_1)\psi_3(\mathbf{r}_2)\psi_1(\mathbf{r}_3) + \zeta\psi_3(\mathbf{r}_1)\psi_2(\mathbf{r}_2)\psi_1(\mathbf{r}_3) + \psi_3(\mathbf{r}_1)\psi_1(\mathbf{r}_2)\psi_2(\mathbf{r}_3)).\end{aligned}$$

The general N indistinguishable particle case results in the following superposition[38]:

$$|\Psi\rangle = |\lambda_1, \lambda_2, ..., \lambda_N\rangle = \frac{1}{\sqrt{N! \prod_{\lambda=0}^{\infty}(n_\lambda!)}} \sum_{\mathcal{P}} \zeta^{(1-\mathrm{sgn}\mathcal{P})/2}\ |\lambda_{\mathcal{P}_1}\rangle \otimes |\lambda_{\mathcal{P}_2}\rangle \otimes ... \otimes |\lambda_{\mathcal{P}_N}\rangle \quad \text{(A.1.1)}$$

where n_λ is the occupation of the state $|\lambda\rangle$ and where the sum runs over all possible permutations of the set $\{\lambda_1, ..., \lambda_N\}$. Here $\mathrm{sgn}\mathcal{P}$ is the sign of the permutation which is 1 [-1] for an even [odd] number of permutations. Clearly, the current approach makes it complicated to work with many particle systems: for $N = 10$ particles, the above equation consists of a few million terms and involve the wave function of each particle, even though they are indistinguishable. This motivates the introduction of second quantisation formalism.

A.1.2. Creation and annihilation operators

For indistinguishable particles, it is convenient to describe a system in the Fock basis[38] (i.e. occupation number representation):

$$|\Psi\rangle = \sum_{\substack{n_1,n_2,...\\ \sum n_i = N}} c_{n_1,n_2,...} |n_1, n_2, ...\rangle$$

where n_i is the occupation of state $|\psi_i\rangle$ and clearly $\sum_i n_i = N$ the number of particles in the system. The annihilation operator $\hat{a}_i$ is defined such that when applied once on $|\Psi\rangle$, the number of particles in the state $|\lambda_i\rangle$ is decreased by one. The creation operator $\hat{a}_i^\dagger$ accordingly adds a particle to the state $|\lambda_i\rangle$. The operators are therefore defined by[38]:

$$\begin{cases} \hat{a}_i |n_1, ..., n_i, ...\rangle = \sqrt{n_i}\zeta^{s_i} |n_1, ..., n_i - 1, ...\rangle & \text{annihilation} \\ \hat{a}_i^\dagger |n_1, ..., n_i, ...\rangle = \sqrt{n_i + 1}\zeta^{s_i} |n_1, ..., n_i + 1, ...\rangle & \text{creation} \\ [\hat{a}_i^\dagger, \hat{a}_j^\dagger]_\zeta = 0,\ [\hat{a}_i, \hat{a}_j]_\zeta = 0,\ [\hat{a}_i, \hat{a}_j^\dagger] = \delta_{ij} & \text{(anti-)commutator relations} \end{cases}$$

where $s_i = \sum_{k=1}^{i-1} n_k$ and where we define $[\hat{A}, \hat{B}]_\zeta \equiv \hat{A}\hat{B} - \zeta\hat{B}\hat{A}$, which clearly serves as commutator $[,]$ for $\zeta = 1$ and anti-commutator $\{,\}$ for $\zeta = -1$. Note that by the Fermi exclusion principle, the occupation n_i for a fermion is mod(2).

Conveniently, for both bosons and fermions, any state $|\Psi\rangle$ can be described only using a successive application of the creation operators on the vacuum state $|0\rangle$, and conversely using the annihilation operator. This formalism allows for describing a quantum state using an operator instead of a wave function. In fact any state may be described by [38]:

$$|\Psi\rangle = |n_1, n_2, ...\rangle = \prod_i \frac{1}{\sqrt{n_i!}} (\hat{a}_i^\dagger)^{n_i} |0\rangle \tag{A.1.2}$$

which, when compared to equation (A.1.1) is much more efficient since one does not bother about the symmetrization of the wave function anymore. Furthermore, this formalism allows for considering systems of infinitely many particles more easily.

A.1.3. Representation of one-body operators

Within this formalism, we are interested in representing some of the common operators: $\hat{T}$, $\hat{p}$, $\hat{\mathbf{S}}$, etc. The latter operators are called one-body operators since they depend on a single radial coordinate $\mathbf{r}$. For this purpose, let $\hat{\mathcal{O}}_1$ be an arbitrary one-body operator for which $\hat{\mathcal{O}}_1 = \sum_{n=1}^{N} \hat{o}_n$, where $\hat{o}_n$ is a single particle operator acting on the n-th particle (e.g. the case for the kinetic energy operator on a many-particle system). Then, the second quantized representation of $\hat{\mathcal{O}}_1$ is given by[38]:

$$\hat{\mathcal{O}}_1 = \sum_{\langle i \rangle j} \langle \lambda_i | \hat{o} \rangle \lambda_j \hat{a}_i^\dagger \hat{a}_j. \tag{A.1.3}$$

A.2. Tight-binding systems

Bloch states and change of basis.— The state of a lattice may be described in momentum space representation (or reciprocal or **k**-space) in which the creation and annihilation operators, now denoted $\hat{a}_{\mathbf{k}}^{\dagger}$ and $\hat{a}_{\mathbf{k}}$, operate identically as detailed in this paragraph. From the Bloch theorem, Bloch wave functions are the solution to the Schrödinger equation for a system periodic in **k**-space, where the single particle Hamiltonian is:

$$H = \frac{\mathbf{p}^2}{2m} + U(\mathbf{r})$$

where $U(\mathbf{r})$ is a periodic potential. The Bloch state for a single band is given by:

$$\psi_{\mathbf{k}} = e^{i\mathbf{k}\cdot\mathbf{R}} u_{\mathbf{k}}(\mathbf{r})$$

where $u_{\mathbf{k}}(\mathbf{r})$ has the same period as the lattice and $U(\mathbf{r})$. The Wannier functions are defined as:

$$\phi_{\mathbf{R}}(\mathbf{r}) = \frac{1}{\sqrt{M}} \sum_{\mathbf{k}\in\mathrm{BZ}} e^{i\mathbf{k}\cdot\mathbf{R}} \psi_{\mathbf{k}}(\mathbf{r}) \tag{A.2.4}$$

where M is the number of primitive unit cells and $\mathbf{R}$ is any lattice vector. One of the properties of Wannier functions is that any Bloch state can be written as a linear combination of Wannier functions. Furthermore, the set of Wannier functions is an orthonormal basis for the state of a band. Thus, using the fact that any state can be written as the sum of projections on Wannier states[50], it can be shown that the relations hold between the annihilation operators from both spaces[51]:

$$\hat{a}_j = \frac{1}{\sqrt{N}} \sum_{\mathbf{k}\in\mathrm{BZ}} e^{i\mathbf{k}\cdot\mathbf{R}_j} \hat{a}_{\mathbf{k}} \quad \text{and} \quad \hat{a}_{\mathbf{k}} = \frac{1}{\sqrt{N}} \sum_{j} e^{i\mathbf{k}\cdot\mathbf{R}_j} \hat{a}_j \tag{A.2.5}$$

where $\mathbf{R}_j$ represents the lattice points in real space. Similar equations for change in basis are obtained for the creation operator by conjugating both sides.

Tight-binding Hamiltonians.— Using equation (A.1.3), the Hamiltonian operator in **k**-space of free non-interacting fermions is given by:

$$\hat{H}_{\text{free}} = \sum_{\mathbf{k},\sigma} \epsilon_{\mathbf{k}} \hat{a}_{\mathbf{k}\sigma}^{\dagger} \hat{a}_{\mathbf{k}\sigma}$$

where σ denotes the spin state ($\sigma \in \{\uparrow, \downarrow\}$ for electrons/holes) and $\epsilon_{\mathbf{k}} = \hbar^2\mathbf{k}^2/2m$ is the energy dispersion relation of a free particle. In real space, the above may be rewritten into[51]:

$$\hat{H}_{\text{free}} = \sum_{l,j,\sigma} \sum_{\mathbf{k}} \epsilon_{\mathbf{k}} e^{i\mathbf{k}\cdot(\mathbf{R}_l - \mathbf{R}_j)} \hat{a}_{l\sigma}^{\dagger} \hat{a}_{j\sigma} \tag{A.2.6}$$

where (A.2.5) was used twice. The term $\hat{a}_{l\sigma}^{\dagger} \hat{a}_{j\sigma}$ annihilates a fermion in position $\mathbf{R}_j$ in spin state σ, and creates a fermion at location $\mathbf{R}_l$ with spin σ: a fermion was transferred from one site to another. The inner term is therefore called the hopping integral:

$$\widetilde{t}_{lj} = \sum_{\mathbf{k}} \epsilon_{\mathbf{k}} e^{i\mathbf{k}\cdot(\mathbf{R}_l - \mathbf{R}_j)}$$

and allows for simplifying equation (A.2.6) into:

$$\hat{H}_{\text{free}} = \sum_{l,j,\sigma} \widetilde{t}_{lj} \hat{a}_{l\sigma}^{\dagger} \hat{a}_{j\sigma}. \tag{A.2.7}$$

The free particle Hamiltonian may be assumed to hold for the hopping of an electron between two sites on a crystal lattice: additionally to an on-site potential V_0, an electron may hop from $l \to j$ with potential t_{lj} and conversely with potential $t_{jl} = t_{lj}^\dagger$. These assumptions form the basis for a nearest-neighbour (NN) tight-binding model and are good approximations for the description of many solids. In particular, a constant hopping potential is assumed:

$$t_{lj} = \begin{cases} -t, & l \text{ and } j \text{ are NN} \\ 0, & \text{else.} \end{cases} . \tag{A.2.8}$$

For a lattice in which there is one atom per unit-cell (i.e. Bravais lattice) the tight-binding Hamiltonian immediately follows:

$$\hat{H}_{\mathrm{TB}} = -t \sum_{\langle l,j \rangle,\sigma} (\hat{a}_{l\sigma}^\dagger \hat{a}_{j\sigma} + \text{h.c.}), \tag{A.2.9}$$

where the index $\langle l, j \rangle$ stands for all possible neighbours and h.c. stands for the Hermitian conjugate of the first term; it can be verified that the hopping term from j to l is the conjugate of the hopping term from l to j. For a crystal with two sublattices A and B (i.e. bipartite lattice) the fermions from both sublattices must be assigned different fermionic operators $\hat{a}_j, \hat{a}_j^\dagger$ and $\hat{b}_j, \hat{b}_j^\dagger$ thus obtaining:

$$\hat{H}_{\mathrm{TB}} = -t \sum_{\langle l,j \rangle,\sigma} (\hat{a}_{l\sigma}^\dagger \hat{b}_{j\sigma} + \text{h.c.}). \tag{A.2.10}$$

Appendix B

Particle-hole symmetry

Consider the Bogoliubov-de Gennes Hamiltonian given by:

$$\hat{H} = \frac{1}{2}(\mathbf{\Psi}^{\intercal})^{\dagger} h_{BdG} \mathbf{\Psi} = \frac{1}{2}(\mathbf{\Psi}^{\intercal})^{\dagger}_{\alpha i \sigma} H_{\alpha i \sigma, \beta j s} \mathbf{\Psi}_{\beta j s}$$

$$h_{BdG} = \begin{pmatrix} H_e & \mathbf{\Delta} \\ \mathbf{\Delta}^{\dagger} & H_h \end{pmatrix}$$

$$\mathbf{\Psi} = (\hat{c}_{1\uparrow}, \hat{c}_{1\downarrow}, \hat{c}_{2\uparrow}, \hat{c}_{2\downarrow}, ..., \hat{c}_{N\downarrow}, \hat{c}^{\dagger}_{1\downarrow}, -\hat{c}^{\dagger}_{1\uparrow}, \hat{c}^{\dagger}_{2\downarrow}, -\hat{c}^{\dagger}_{2\uparrow}, ..., -\hat{c}^{\dagger}_{N\uparrow})^{\intercal}$$

where α (β) indicates the sublattice corresponding to the site i (j) with spin σ (s) and where H_e and H_h denote the single-particle Hamiltonians for electron and hole respectively. We are looking to rewrite the Hamiltonian using the particle-hole symmetry operator. First, consider the operator which exchanges $\mathbf{\Psi}$ and $\mathbf{\Psi}^{\dagger}$:

$$\mathbf{\Psi}^{\dagger} = \tau_y \otimes \mathbb{1}_N \otimes \sigma_y \mathbf{\Psi} \equiv \mathcal{O}\mathbf{\Psi}.$$

Thus we can rewrite the first equation using this operator:

$$\begin{aligned} \hat{H} &= \frac{1}{2}(\mathbf{\Psi}^{\dagger})^{\intercal} h_{BdG} \mathbf{\Psi} \\ &= \frac{1}{2}\mathbf{\Psi}^{\intercal}(\mathcal{O}^{\intercal} h_{BdG} \mathcal{O})\mathbf{\Psi}^{\dagger} \\ &= \frac{1}{2}(\mathbf{\Psi}_{\beta j s})(\mathcal{O}H\mathcal{O})_{\beta j s, \alpha i \sigma}(\mathbf{\Psi}^{\dagger})_{\alpha i \sigma} \\ &= -\frac{1}{2}(\mathbf{\Psi}_{\alpha i \sigma})(\mathcal{O}H\mathcal{O})^{\intercal}_{\alpha i \sigma, \beta j s}(\mathbf{\Psi}^{\dagger})_{\beta j s} \end{aligned}$$

where it was used that $\mathcal{O}$ is Hermitian and in the last rule the fermionic commutation relations. It follows that:

$$-\mathcal{O} h^{\intercal}_{BdG} \mathcal{O} = h_{BdG}$$

which can also be written:

$$\mathcal{P} h_{BdG} \mathcal{P}^{-1} = -h_{BdG}$$

with $\mathcal{P} = \mathcal{P}^{-1} = \mathcal{O}\mathcal{K}$ and $\mathcal{K}$ the operator of complex conjugation. This result can be further developed into the blocks of the Hamiltonian thereby obtaining:

$$H_h = -\mathcal{T} H_e \mathcal{T}^{-1}$$

with $\mathcal{T} = -i\mathbb{1}_N \otimes \sigma_y \mathcal{K}$ and $\mathcal{T}^{-1} = i\mathbb{1}_N \otimes \sigma_y \mathcal{K}$. Therefore, the Bogoliubov-de Gennes Hamiltonian can be written as:

$$h_{BdG} = \begin{pmatrix} H_0 - \mu & \mathbf{\Delta} \\ \mathbf{\Delta}^{\dagger} & \mu - \mathcal{T} H_0 \mathcal{T}^{-1} \end{pmatrix}.$$